Tunable photoluminescence of $CaCu_3Ti_4O_{12}$ based ceramics modified with tungsten

H. Moreno [a, *], J.A. Cortés [a], F.M. Praxedes [a], S.M. Freitas [b], M.V.S. Rezende [b], A.Z. Simões [a], V.C. Teixeira [c], M.A. Ramirez [a]

[a] Sao Paulo State University — UNESP, Faculty of Engineering of Guaratingueta, Av. Dr. Ariberto Pereira da Cunha 333, Portal das Colinas, 12516-410, Guaratingueta, SP, Brazil
[b] Federal University of Sergipe (UFS) — Center for Exact Sciences and Technology (CCET), Department of physics, Marechal Rondon s/n, Jardim Rosa Elze, 49100-000, Sao Cristovao, SE, Brazil
[c] Brazilian Synchrotron Light Laboratory (LNLS), Brazilian Center for Research in Energy and Materials (CNPEM), 13083-970, Campinas, SP, Brazil

ARTICLE INFO

ABSTRACT

$CaCu_3Ti_4O_{12}$ (CCTO): x% W (x = 0.00, 0.02, 0.05, 0.10, 2.50, and 5.00) powders were prepared via solid-state reaction. The effect of W addition in the (micro)structure and optical properties was analyzed using computing simulations and experimental techniques. The widespread application of perovskite-light-emitting diodes (PeLEDs), photovoltaic devices, and photocatalysis is limited by the intrinsic instability of the perovskite materials (e.g., metal halides), compromising operational efficiency, and pushing for the development of novel perovskite materials. The Rietveld analysis and XPS results confirm the presence of W^{5+}, Ti^{3+}, and Cu^+ ions in all samples of the $CaCu_3Ti_4O_{12}$: x% W system, leading to structural changes that strongly influence the PL response of the material. Based on a correlation approach, a practical model explaining the relationship between electronic defects and photoluminescent (PL) emissions in the CCTO system is proposed. On samples x = 0.00, 0.10, and 5.00, red PL emissions are due to the presence of metal vacancies, and deep-level defects, while blue PL emissions on samples x = 0.02, 0.05, and 2.50 are associated with shallow defects. Thus, our research shows evidence that $CaCu_3Ti_4O_{12}$ (CCTO): W ceramic systems may be promising to photonics applications.

© 2020 Elsevier B.V. All rights reserved.

1. Introduction

$CaCu_3Ti_4O_{12}$ (CCTO) is a multifunctional ceramic system whose applications range from microelectronics (i.e., memory-based devices and capacitors) [1,2], non-ohmic devices [3,4], sensors [5–7] to optoelectronics [8–12] and magnetism [13,14]. The multifunctional properties associated with this class of materials arise from an intrinsic ability of perovskite structures to tolerate slight deviations and ionic combinations [11]. The development of functional materials is governed by a growing demand for the miniaturization of electronic devices [13], which depends fundamentally on the dielectric permittivity and dielectric loss of materials [15]. Since Subramanian et al. [16] first reported the giant dielectric constant (ε ~ 10^4 - 10^5) of $CaCu_3Ti_4O_{12}$ (CCTO) in 2000, it stood out. Additionally, CCTO exhibits excellent physicochemical properties and thermal stability over a wide range of temperatures, which derives from its perovskite structure with general formula ABO_3 [17,18]. CCTO presents a distorted perovskite structure with stoichiometric formula $(AA')BO_3$. Inclined TiO_6 octahedra originate from the Jahn-Teller effect [4], which explains the square-planar and dodecahedral coordination of the Cu^{2+} and Ca^{2+} ions, respectively. Hence, a more compact crystal structure forms in comparison to other common perovskites with stoichiometric formula ABO_3 (e.g., $CaTiO_3$, $SrTiO_3$), in which the Ti–O bonds are tensed and more susceptible to electric field effects.

Optoelectronic properties of CCTO can be tuned using several specific strategies, such as transition metal [10,19–22] and/or rare earth element [23,24] doping; ceramic composite processing [18,25–27]; and alternative methods of synthesis (solid-state reaction, sol-gel method, polymeric precursor, etc.) [14,15,19,28–30]. The use of different methods to synthesize CCTO can produce particles of different shapes and sizes, which has a direct influence on the Photoluminescent (PL) response. Additionally, PL is highly dependent on the structural symmetry, tilting and/or rotating of

the coordination polyhedra, which can influence the electronic structure of the material (e.g., bandgap narrowing) as a consequence of point defects (e.g., oxygen or metal vacancies) [31]. The degree of charge transfer between $[TiO_6]$, $[TiO_5.V_O^\bullet]$, and $[TiO_5.V_O^{\bullet\bullet}]$ and the lattice modifier complex clusters $[CaO_{11}.V_O^{\bullet\bullet}]$ can be tailored by the introduction of intermediary energy levels within the bandgap region [32–35]. This relation was confirmed by Orrego et al. [28] for Sr^{2+}-doped CCTO, in which the complex clusters $[TiO_5.V_O^\bullet]$ and $[TiO_5.V_O^{\bullet\bullet}]$ were identified. The authors established a correlation between the presence of defects and PL emissions: (1) in the violet region, which is related to shallow defects; (2) in the green region, associated with a decrease in the density of trapped charges, and in particle size; and (3) a red-shift, evident with the increase in Sr^{2+} content, was associated with deep-level defects in the CCTO electronic structure. The structural defects induced in the system led to the formation of intermediary levels between the valence and conduction bands. The application of CCTO in optical devices depends on PL emission characteristics, which include: efficiency, wavelength range, and time decay, etc. However, the mechanisms related to PL emission are yet to be fully understood.

The growing demand for sustainable energy sources and energy-efficient devices has pushed the development of PeLEDs [36–38] and photovoltaic devices [39,40] over the last few years. Furthermore, CCTO-based ceramics have proved to be an efficient alternative for photocatalysis, which offers the possibility to degrade water pollutants into environmentally-benign chemicals at a low cost using the energy of the sun [39,41–43]. Perovskite materials for application in PeLEDs and photovoltaic devices (e.g., organic fluorescent and phosphorescent molecules, metal halide perovskites, etc.) stand out because of their high efficiency, low fabrication cost, high purity, and widely tunable light emission, etc. The intrinsic instability of perovskite materials, such as organic molecules and metal halides, under thermal heating, light, and electric field poses an intrinsic threat to the operational efficiency and, thus, requires the development of novel perovskite materials [44–46]. Since the first room-temperature PeLED, $CH_3NH_3PbI_{3-x}Cl_x$, was developed by Tan et al. [47] in 2014, much effort has been placed in optimizing perovskites for light-emitting diode (LED) applications [36–38]. According to the literature, W^{6+}-doping in CCTO systems ($CaCu_3Ti_{4-x}W_xO_{12}$) [48,49] leads to the formation of titanium and oxygen vacancies, which are formed within the bandgap region during the thermal treatment due to the oxidizing nature of tungsten, and could influence the dynamics of PL emissions as a result of these changes in the electronic structure of CCTO. After a careful literature review, no reports were found regarding the effect of tungsten (W) on the PL response of CCTO.

Therefore, in this paper, we focus on the study of $CaCu_3Ti_4O_{12}$: x% W (x = 0.00, 0.02, 0.05, 0.10, 2.50 and 5.00) ceramic powder prepared, adding W^{6+} ions to CCTO, via solid-state reaction in terms of (micro) structure and optical properties. The structural defects responsible for the optical response were evaluated, and structural simulations based on atomistic modeling were performed to predict the kind of defects induced in the structure considering the addition of W in the CCTO host lattice. This work provides theoretical-experimental evidence to support the use of ceramics based on CCTO in optoelectronics and shows that it is possible to produce PeLEDs with tunable PL intensity and wavelength over the visible spectrum.

2. Experimental procedure

2.1. Synthesis

$CaCu_3Ti_4O_{12}$: x% W (x = 0.00, 0.02, 0.05, 0.10, 2.50, 5.00) ceramic powders were prepared via solid-state reaction using stoichiometric proportions of $CaCO_3$ (99.9%; Sigma-Aldrich), TiO_2 (99.9%; Sigma-Aldrich), and CuO (99.9%; Sigma-Aldrich) as starting reagents. The W ions were added to the CCTO system in the form of WO_3 (99.9%; Sigma-Aldrich) powder. The reagents were mixed thoroughly for 24 h in an isopropyl alcohol suspension using yttrium-stabilized zirconia spheres as grinding medium. After milling, the mixture was taken to a fume hood for 2 h and then dried in an oven for 12 h at 100 °C, deagglomerated in an agate mortar, and sift in a 200-mesh sieve in order to obtain a homogeneous powder. Subsequently, the samples were calcined at 900 °C for 12 h under air atmosphere using a heating rate of 5 °C/min, as determined by thermogravimetric analysis (TG-DTG) (Figs. S1–S2) [50]. Finally, the samples were submitted to milling for 12 h for eliminating neck-like junctions between particles formed during calcining.

2.2. Characterization

2.2.1. (Micro)structural characterization

X-Ray Powder Diffraction (XRPD) was performed in a Bruker (model D8 Advance Eco) diffractometer operating at 40 kV/25 mA and using the copper K_α radiation ($\lambda \approx 1.5406$ Å). The data were collected in the range of $10 = \theta \le 100°$ with a step of 0.02°, a collection time of 10 s/point, and a receiving slit of 0.6 mm. The crystal structure of the powders was refined using the Rietveld method [51] in the software Topas V.5 in its academic version [52]. The phases were quantified, and the statistical parameters associated with the crystalline structure (R_{Bragg}, R_{wp}, R_{exp}, and χ^2) estimated. The R_{Bragg} is a mathematical function that depends on peak intensity, and which is intrinsically related to the crystal structure of a material. Thus, R_{Bragg} represents the fitting between the experimental and calculated data; hence $R_{Bragg} = 1$ means a perfect fitting [53]. Among the Rietveld parameters, three stand out: (1) R_{wp} measures the refinement convergence for the observed data; (2) R_{exp} represents the expected value for R_{wp}; and (3) χ^2 expresses the R_{wp}: R_{exp} ratio. The statistical parameters estimate the confidence of the refinement, and the unit represents the ideal value. It is important to keep in mind that the parameters R_{wp}, R_{exp}, and χ^2 provide an evaluation regarding the quality of refinement, taking into consideration only the comparison of profiles. On the other hand, R_{Bragg} enables the assessment of the structural model refined.

In order to determine the crystalline phases present on samples, the experimental data were fitted with standards patterns available at the Inorganic Crystal Structure Database (ICSD). For all samples, a Chebychev polynomial function of order 5 was used for the background to refine the structures. In order to determine lattice deviations with higher confidence, additional XRPD measurements were carried out on a Debye-Scherrer geometry, with a Si (111) monochromator ($\lambda \approx 1.034$ Å) operating at 12 keV (100 mA) with a step size of 3×10^{-4}. The XRPD diffractograms were collected at room temperature with rotation (300 rpm) using the MYTHEN 24 K system from Dectris® at the X-Ray Diffraction (XRD1) beamline from the Brazilian Synchrotron Light Laboratory (LNLS) [54,55]. The elemental composition of the sample was examined by X-ray photoelectron spectroscopy (XPS) using the UNI-SPECS UHV system. The X-ray tube with Al-Kα radiation (hν = 1254.6 eV) was used, and the Shirley method was applied to subtract the inelastic noise associated with the high-resolution spectra obtained for C 1s, O 1s, Ti 2p, Cu 2p, Ca 2p, W 4d. The spectra were deconvoluted using the Voigtian function with a combination (70% Gaussian and 30% Lorentzian). The full width at half-maximum of the was determined with a resolution of 0.1 eV. Raman spectroscopy was carried out using a Renishaw (inVia Qontor) Raman scattering microscope using an argon-ion laser with a wavelength of 532 nm. For each sample, the average spectrum was obtained from three

sequential scans with a spectral step of 1.13 cm^{-1} over the range of 150−1200 cm^{-1}. For the analysis, the samples were deagglomerated in an agate mortar and placed over a glass substrate.

X-ray Absorption (XAS) data were collected around the Ti K-edge (E$_0 \approx$ 4966 eV) at the X-ray Absorption and Fluorescence Spectroscopy (XAFS1) line at LNLS. The experiment was performed on transmission mode using thin membranes. Ti-foil standard was used to calibrate the monochromator. TiO$_2$ and Ti$_2$O$_3$ were used as reference materials for the measurements [56]. Three sequential scans were run for each sample in order to optimize the signal-to-noise ratio. The experimental data were treated using the software ATHENA [57].

A Field-emission-gun coupled scanning electron microscope (FEG-SEM) on a Supra 35-VP (Carl Zeiss) was used to evaluate the morphology of the particles. The particle size distribution was determined using the software ImageJ [58,59].

2.2.2. Computational method

Atomistic simulation based on the Coulombic and the short-range term of the Buckingham form (Eq. (1)) was used to perform static simulations, based on the Born model, to investigate the incorporation of W ions within the CCTO structure.

$$U^{Buckinham} = A \exp\left(\frac{-r_{ij}}{\rho}\right) - \frac{C}{r_{ij}^6} \tag{1}$$

where $U^{Buckinhanm}$ is the Buckingham interatomic potential, A represents the repulsion between two ions i and j separated by a distance r, which is related to the size and "hardness" of the ions, ρ is the minimum energy distance, and C is the term included to model the dispersion. The energy minimization procedure, which adjusts ionic positions in order to obtain the lowest energy structure, was adopted. The core-shell model is included to describe the ionic polarizability effect, in which the anions are divided into a massive core and a massless shell connected to a harmonic spring [60]. Defect calculations were performed using the Mott-Littleton methods, in which the crystal lattice is partitioned into a region in which relaxations close to the defect are treated explicitly, and the remainder of the lattice is treated using quasi-continuum methods [61]. For all calculations, the General Utility Lattice Program (GULP) code was used [62].

2.2.3. Optical characterization

The Ultraviolet−visible (UV−visible) spectra for all samples were obtained using a Cary 50 Bio (Varian, USA) spectrophotometer in the diffuse reflection mode. The optical bandgap energy (E_{gap}) also referred to as the fundamental absorption onset of the host lattice was estimated for all samples using the Kubelka-Munk equation (Eq. (2))

$$\alpha h\nu = C_1 \left(R_\infty \left(h\nu - E_{gap}\right)^n\right) \tag{2}$$

where α is the linear absorption coefficient, h Planck's constant ($h = 4.1357 \times 10^{-15}$ eV s^{-1}), ν the frequency of the light, C_1 is a constant, R_∞ is the reflectance when the sample is taken as infinitely thick, and E_{gap} corresponds to the gap energy of the material. Additionally, the variable n can assume specific values depending on the electronic transition ($n = \frac{1}{2}$, 3/2, 2 or 3 for direct allowed, indirect forbidden, direct forbidden, and indirect forbidden, respectively) [63,64].

The photoluminescent response was measured using an ISS (model PC1) with a xenon lamp of 300 W as the excitation source, a step of 0.5 nm, and optical slits of 1 mm, equipped with R928 photomultiplier (Hamamatsu). The PL data were deconvoluted

based on a Gaussian function. The radiant efficiency (η_r) of a semiconductor describes the capacity of the material to convert optical power (photons) into light output capability. Eq. (3) was used to estimate the radiant efficiency for all samples.

$$\eta_r = \frac{E}{A} \tag{3}$$

where E corresponds to the area under the curve on the excitation spectrum, and A is the area under the curve on the emission spectrum for each of the samples [65]. Finally, the PL emission spectra for each sample (x = 0.00−5.00) was converted into a point in the chromaticity diagram (CIE 1931) using the software GoCIE V2 [66]. The correlated color temperature (CCT) for each of the samples was calculated according to Eq. (4) [67]:

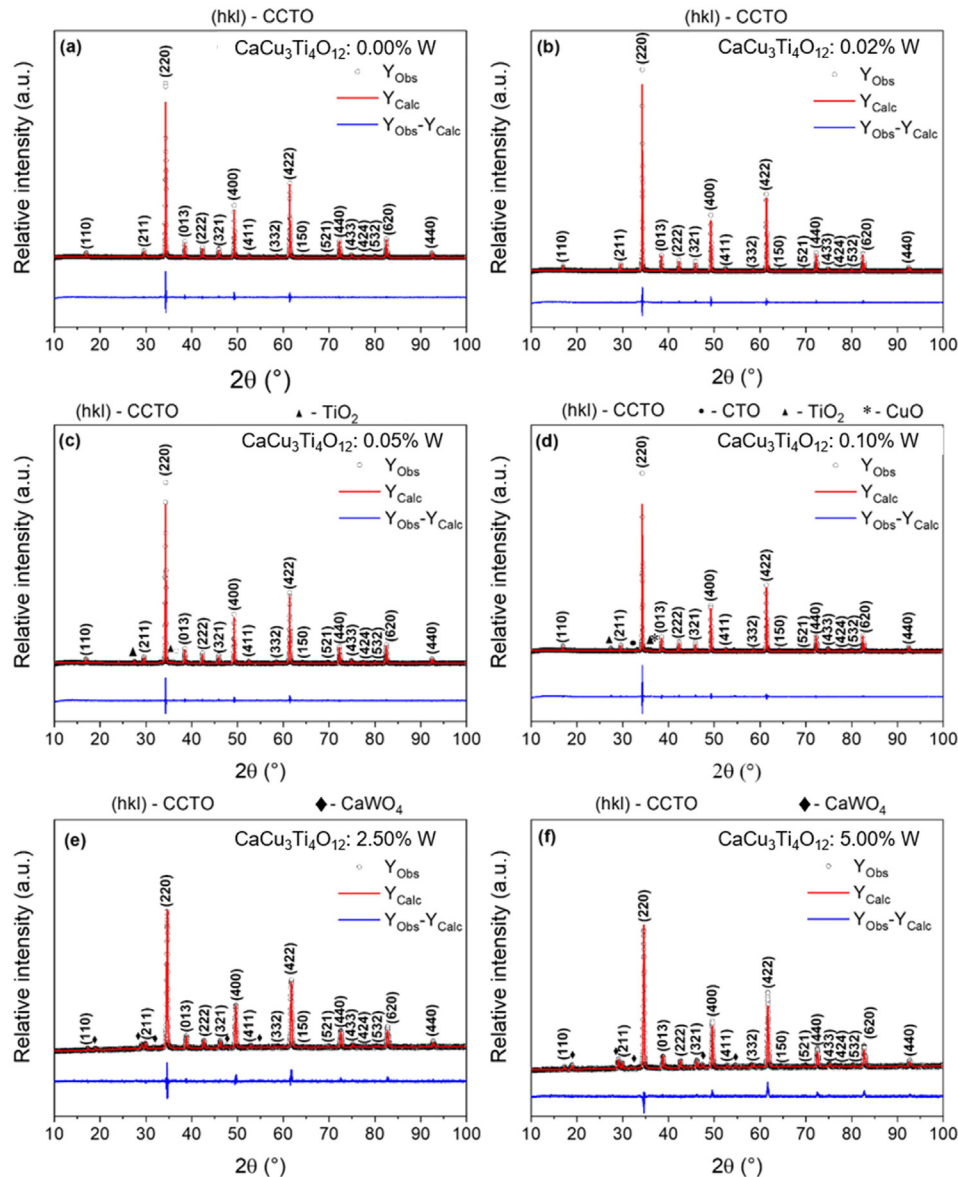$$CCT = -449n^3 + 3525n^2 + 6823.2n + 5520.3 \tag{4}$$

where $n = \frac{x - x_e}{y - y_e}$, $x_e = 0.332$ and $y_e = 0.186$, and x and y correspond to the coordinates for each sample in the CIE diagram.

3. Results and discussion

3.1. (Micro)structural characterization

Fig. 1(a−f) shows the XRPD patterns treated using the Rietveld method. Accordingly, the structural and Rietveld parameters acquired for all samples (x = 0.00−5.00) are shown in Table 1. For the samples x = 0.00 and x = 0.02 all peaks were indexed by the CCTO phase (ICSD #259849) with cubic perovskite-type structure and space group Im-3 [4]. For samples x = 0.05−5.00, ceramic composites were formed. For sample x = 0.05 the TiO$_2$ phase, with rutile structure (ICSD #33840, space group P4$_2$/mnm) was identified. In addition to the phases CCTO and TiO$_2$, sample x = 0.10 presented the following phases: CuO, with tenorite structure (ICSD #69094, space group C12/c); and CaTiO$_3$, with orthorhombic perovskite structure (ICSD #74213, space group Pbnm). The formation of these phases is associated with the incorporation of the W ions at the Ti site, which is favored by their close ionic radii ($R_{W^{6+}}$ = 0.600 Å and $R_{Ti^{4+}}$ = 0.605 Å) [68]. However, the different oxidation states of tungsten and titanium ions result in the dissociation of the CCTO system in CTO, TiO$_2$, and CuO. In the CTO phase, it is necessary to consider that for a low W: Ti substitution ratio, the system charges will be compensated by the formation of defects. On samples x = 2.50 and 5.00, further addition of tungsten ions to the CCTO system produces the CaWO$_4$ phase with scheelite structure (ICSD #60549, space group I4$_1$/a) by a combination of the excess Ca and W ions. Therefore, the solubility limit for the W ions in the CCTO structure based on the Hume-Rothery rules [69] lies between x = 0.10 and x = 2.50. Additionally, the excess Cu ions in the system are incorporated into the Ca sites of the CaWO$_4$ structure, originating the system Ca$_{1-x}$Cu$_x$WO$_4$. This hypothesis explains the disappearance of the CuO phase in samples x = 2.50 and 5.00 and is confirmed by the Rietveld results (Table 2). The Rietveld parameters, $1.28 < \chi^2 < 2.62$ and $1.16 < R_{bragg} < 7.14$, indicate high reliability of the data obtained by means of the refinement operations [53]. The Rietveld refinement also indicates that the W ions incorporated in the CCTO structure occupy the Ti sites, as shown in Table 2.

Fig. 2 (a) depicts the XRPD patterns obtained using synchrotron radiation ($\lambda \approx$ 1.034 Å). The narrow peaks in the diffractogram reveal a material with high crystallinity. Corroborating the results obtained using Rietveld refinement, samples x = 0.00 and 0.02 revealed only the CCTO phase while ceramic composites with the phases TiO$_2$, CaTiO$_3$, CuO, and CaWO$_4$ were obtained in samples

Fig. 1. XRPD patterns of the system $CaCu_3Ti_4O_{12}$: x% W for samples (a) x = 0.00, (b) x = 0.02, (c) x = 0.05, (d) x = 0.10, (e) x = 2.50, and (f) x = 5.00 fitted using the Rietveld refinement method.

x = 0.05−5.00. Fig. 2 (b) highlights a shift of the peak relative to the crystallographic plane (220) towards smaller Bragg angles (2θ). This peak displacement is associated with strain in the main phase (CCTO) and indicates the lattice expansion as a result of the incorporation of W in the CCTO structure. The lattice distortion is due to a sum of factors including the simultaneous presence of W^{6+} ($R_{W^{6+}} = 0.600$ Å) and W^{5+} ($R_{W^{5+}} = 0.620$ Å) ions in a ~45:55 ratio on the surface, according to the XPS analysis, incorporated at the Ti sites ($R_{Ti^{4+}} = 0.605$ Å). Furthermore, the oxidative nature of tungsten induces the reduction of titanium and copper ions into Ti^{3+} ($R_{Ti^{3+}} = 0.670$ Å) and Cu^+ ($R_{Cu^+} = 0.600$ Å; $R_{Cu^{2+}} = 0.570$ Å) ions in the CCTO structure [49,70,71]. The geometric parameters (Table 1) obtained from the Rietveld refinement confirm the lattice expansion indicated in Fig. 2(a and b). In order to fully understand the lattice distortion associated with ionic substitutions in CCTO, in this case, the incorporation of W ions at the Ti sites, it is also necessary to observe the correlation between unit cell volume and W occupancy factor, shown in Table 2. Analogously, on Fig. 2 (c), for

samples x = 2.50 and 5.00, it can be observed that the peak relative to the plane (112) of the phase $CaWO_4$ shifts towards higher 2θ values, which can be associated with contraction of the lattice due to the incorporation of Cu ions ($R_{Cu^+} = 0.600$ Å; $R_{Cu^{2+}} = 0.570$ Å) at the Ca sites ($R_{Ca^{2+}} = 1.000$ Å) [68] in the system $Ca_{1-x}Cu_xWO_4$, as indicated by the Rietveld analysis (Table 2).

Fig. 3(a−d) shows the W 4d XPS spectra for all the studied samples. The W $4d_{5/2}$ spectra were adjusted using two components, WO_3 (W^{6+}) at ~249 eV and W_2O_3 (W^{5+}) at ~246.4 eV. The W^{5+}:W^{6+} ratio remains approximately constant (~55:45) for all samples (x = 0.05−5.00). Fig. 3(e−i) displays the Ti 2p XPS spectra for all samples of the $CaCu_3Ti_4O_{12}$: x% W system (x = 0.00−5.00). Two peaks were identified at ~465 eV and ~459 eV, each of which was deconvoluted into two spin-orbit doublet Ti state peaks, indicating the simultaneous existence of Ti^{3+} and Ti^{4+}, which are related to titanium in the form of TiO_2 and Ti_2O_3, respectively [72]. The fitting parameters for the peak fitting of Ti $2p_{3/2}$ peak for all the samples are shown in Table 3. The main peak at ~459 eV can be ascribed to

Table 1
Structural data and Rietveld parameters for all samples of the system $CaCu_3Ti_4O_{12}$: x% W (x = 0.00−5.00). \

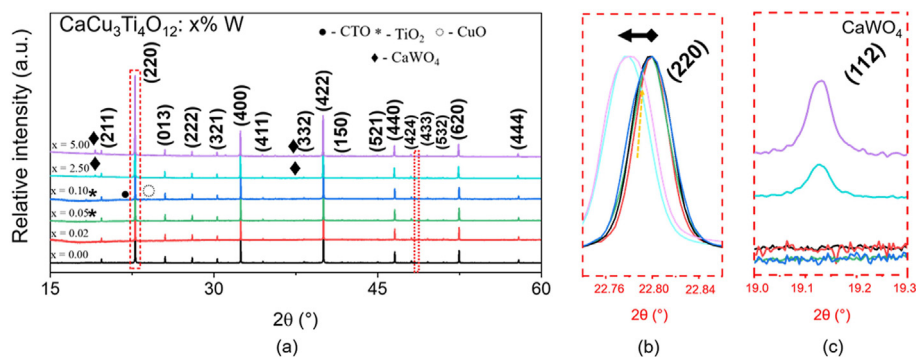| Samples	$CaCu_3Ti_4O_{12}$			TiO_2			$CaTiO_3$			CuO			$CaWO_4$			Rietveld parameters			
	V (Å³)	phase (%)	R_{Bragg}	V (Å³)	phase (%)	R_{Bragg}	V (Å³)	phase (%)	R_{Bragg}	V (Å³)	phase (%)	R_{Bragg}	V (Å³)	phase (%)	R_{Bragg}	R_{exp}	R_{wp}	R_p	χ^2
x = 0.00	404.0	100.0	1.16	–	–	–	–	–	–	–	–	–	–	–	–	3.79	5.82	4.41	1.54
x = 0.02	404.2	100.0	1.01	–	–	–	–	–	–	–	–	–	–	–	–	3.66	6.07	4.59	1.66
x = 0.05	403.95	97.2	1.13	63.83	2.8	3.59	–	–	–	–	–	–	–	–	–	3.82	5.71	4.33	1.49
x = 0.10	404.2	92.3	1.02	62.47	2.1	1.25	223.5	2.2	1.12	81.66	3.4	0.658	–	–	–	3.70	6.00	4.47	1.62
x = 2.50	405.1	98.4	3.79	–	–	–	–	–	–	–	–	–	314.1	1.6	0.92	4.62	5.86	4.60	1.27
x = 5.00	405.2	96.5	4.707	–	–	–	–	–	–	–	–	–	314.1	3.5	1.60	4.33	5.96	4.74	1.24

the Ti^{4+} ions, and the secondary peak fitted at ~457 eV in the Ti $2p_{3/2}$ may be associated with the Ti^{3+} ions. It is possible to observe a tendency towards the reduction of Ti^{4+} into Ti^{3+} ions with higher tungsten content, which may be related to the oxidative nature of W [49]. Additionally, for all samples, the Cu 2p XPS spectra (Fig. 3j-n) shows an asymmetric peak corresponding to Cu $2p_{3/2}$ spin-orbit doublets (~933 eV) and its satellite peak (~941 eV), which is consistent with the presence of Cu^{2+}/Cu^+ ions in the CuO lattice [72−74]. The Cu 2 $p_{3/2}$ peak was deconvoluted into two peaks associated with Cu^{2+} species in the form of CuO (~934.7 eV) and Cu^+ species in the form of Cu_2O (~932.5 eV) [74,75]. The addition of W to CCTO caused an increase in the concentration of Cu^+ ions, as shown in Table 3. Hence, the Cu^{2+}/Cu^+ ratio decreases significantly with the addition of tungsten to CCTO. The full scan XPS profiles obtained for all samples of the $CaCu_3Ti_4O_{12}$: x% W (x = 0.00−5.00) system (Fig. S3) shows the various elements present as a function of their binding energy. It is possible to observe the presence of O 1s components at ~529 eV and ~530.8 eV related to O−Cu/O−Ca and O−Ti bonds (O^{2-}), respectively, in the CCTO structure. The Ca $2p_{3/2}$ and Ca $2p_{1/2}$ (~348 eV) spin-orbit doublets are associated with Ca^{2+} ions in the form of CaO.

Table 2
Unit cell volume and occupancy factor of the ions W and Ti in the B site (0.250. 0.250. 0.250) in the CCTO structure; and unit cell volume and occupancy factor of the ions Cu and Ca in the A site (0.000. 0.250. 0.625) in the $CaWO_4$ structure for all samples of the system $CaCu_3Ti_4O_{12}$: x% W (x = 0.00−5.00).

Samples	$CaCu_3Ti_4O_{12}$			$CaWO_4$		
	V (Å³)	Occ. W (%)	Occ. Ti (%)	V (Å³)	Occ. Cu (%)	Occ. Ca (%)
x = 0.00	404.0	0.00	100.00	–	–	–
x = 0.02	404.2	2.88	97.12	–	–	–
x = 0.05	404.0	1.88	98.00	–	–	–
x = 0.10	404.2	3.33	97.88	–	–	–
x = 2.50	405.1	1.75	98.25	314.1	40.06	59.94
x = 5.00	405.2	1.92	98.15	314.1	25.45	74.55

Fig. 4 (a) shows the Raman spectra collected at room temperature for all samples of the system $CaCu_3Ti_4O_{12}$: x% W. According to the group theory, there are 23 vibrational groups possible for CCTO: 2 A_g; 2 A_u; 2 E_g; 2 E_u; 4 F_g; and 11 F_u, of which eight (2 A_g + 2 E_g + 4 F_g) are Raman active [76−78]. In all samples, the vibrational modes P_1, P_3, P_4, P_6, and P_7 associated with the $[TiO_6]$ cluster in the CCTO structure, were identified at 286 ($F_g(1)$), 401 ($F_g(2)$), 445 ($A_g(1)$), 509 ($F_g(2)$), and 572 ($A_g(2)$) cm^{-1}, respectively [76]. The mode P_7 is associated with the asymmetric movement of coplanar oxygen ions around the centralized Ti^{4+} ions in the TiO_6 octahedra [77]. Modes P_4 (445 cm^{-1}), P_6 (506 cm^{-1}), and P_8 (612 cm^{-1}) are generated by the interaction between the octahedra joined by the vertex (folding, twisting, etc.). The modes P_2, P_5, P_9−P_{11} are associated with the $[WO_4]$ cluster present in the $Ca_{1-x}Cu_xWO_4$ structure [79−82]. Higher tungsten content in the CCTO structure leads to an increase in the intensity of the mode associated with mode P_5 and the reduction in the intensity of mode P_8, which indicates the2 formation of oxygen vacancies associated with the TiO_6 cluster [77,83]. On samples x = 2.50−5.00, with higher W content, the vibrational mode P_{10} at 838 cm^{-1} ($B_g(5)$) is associated with the antisymmetric stretching of O−W − O bonds [79−82]. Sample x = 5.00 reveals the vibrational modes P_2 (333 cm^{-1}), P_9 (778 cm^{-1}), and P_{11} (909 cm^{-1}). Mode P_2 is related to the symmetries $A_g(2)$ + $B_g(3)$ combined, which can be assigned to the symmetric bending of the $[WO_4]$ tetrahedra. An increase in the intensity of the peak related to mode P_2 indicates disorder in the system. Additionally, the mode P_{11} related to the symmetry $A_g(3)$ can be associated with the symmetric stretching of W−O bonds [79−82]. Fig. 4 (b) shows that increasing tungsten content it is possible to observe a shift towards higher wavenumbers on modes P_6 and P_7, which is associated with lattice deformation. These results are consistent with the Rietveld analysis and confirm the expansion of the unit cell as a result of the incorporation of W ions at the Ti sites, which is evidenced by the occupancy factor results (Table 2) [84]. Analogously, mode P_{10} shifts towards lower

Fig. 2. (a) XRPD patterns of the system $CaCu_3Ti_4O_{12}$: x% W measured using synchrotron radiation for all samples (x = 0.00−5.00). The insets show an expanded view of the planes (b) (220) in the CCTO and (c) (112) in the $CaWO_4$ structures, respectively.
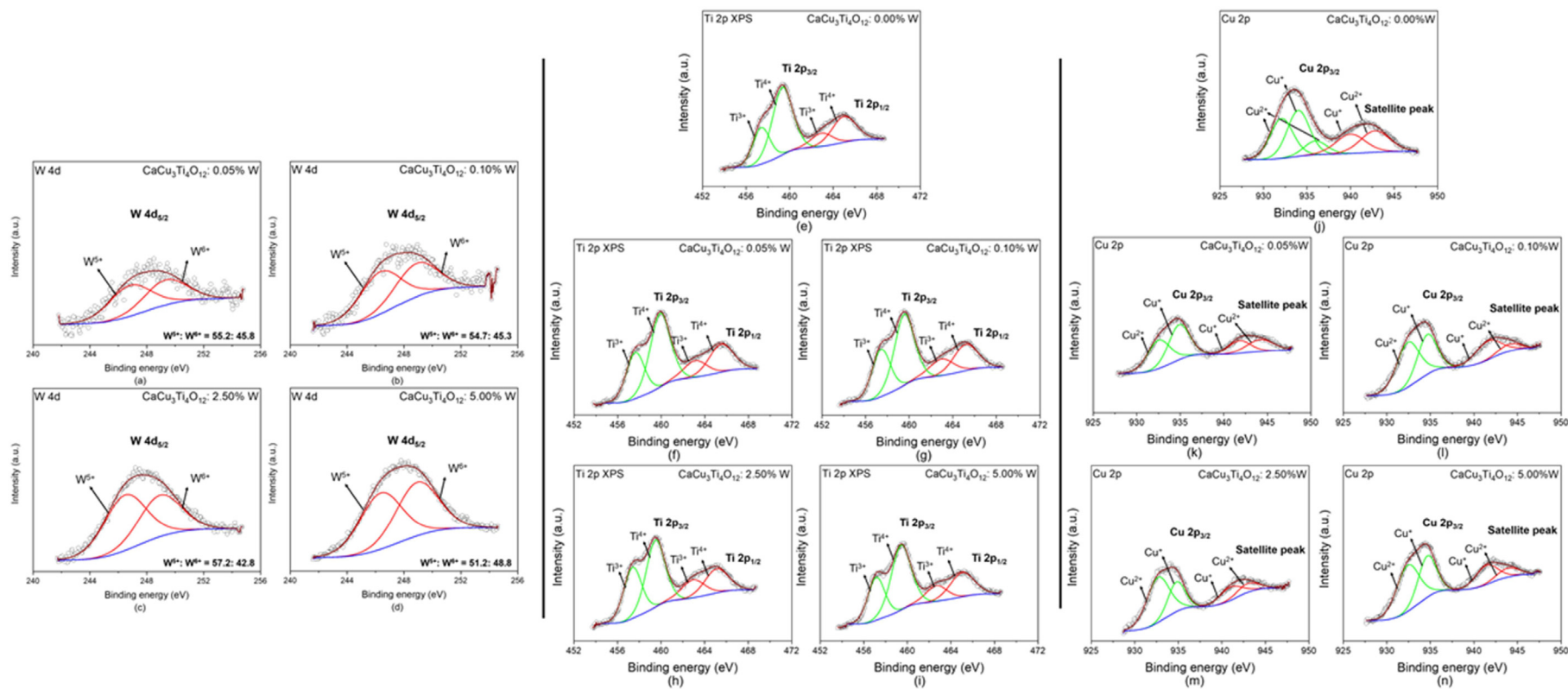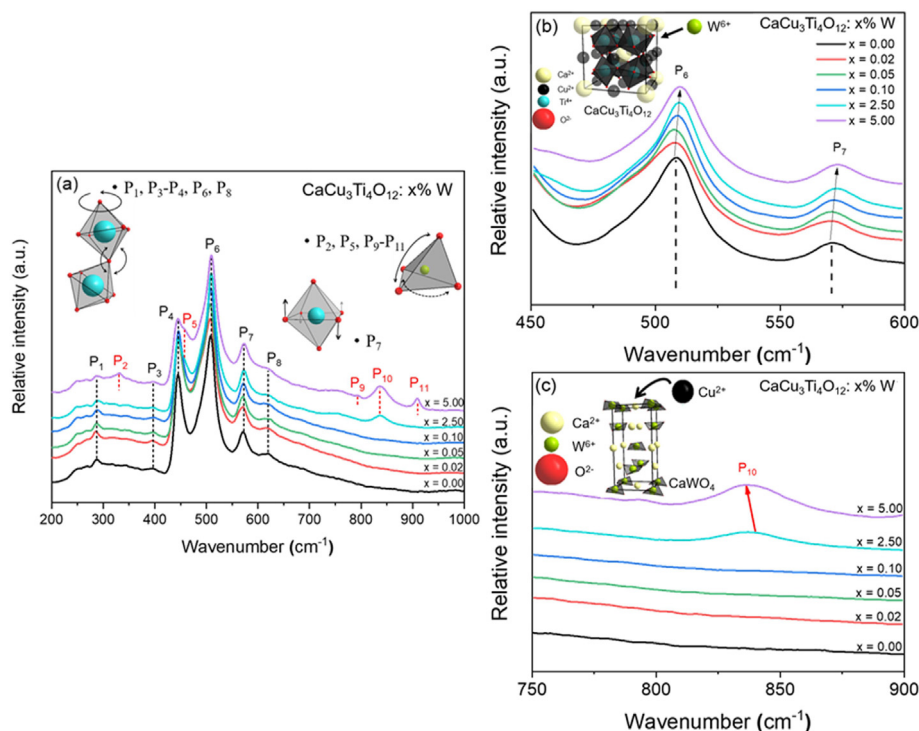
Fig. 3. (a−d) W 4d, (e−i) Ti 2p and (j−n) Cu 2p XPS peak fitting for the $CaCu_3Ti_4O_{12}$: x% W (x = 0.00−5.00) system.

Table 3
XPS fitting parameters for the system $CaCu_3Ti_4O_{12}$: x% W (x = 0.00−5.00).

	Samples	Peak centers (eV)		Peak centers (eV)		Ti^{4+}: Ti^{3+} ratio (%)
		P_1 Ti $2p_{3/2}$ (Ti^{4+})	P_2 Ti $2p_{3/2}$ (Ti^{3+})	P_1 Ti $2p_{1/2}$ (Ti^{4+})	P_2 Ti $2p_{1/2}$ (Ti^{3+})	
Ti 2p	x = 0.00	459.3	457.5	465.0	462.9	68.7: 31.3
	x = 0.02	–	–	–	–	–
	x = 0.05	459.9	457.6	465.5	463.1	63.7: 36.2
	x = 0.10	459.5	457.4	465.2	463.0	61.8: 38.2
	x = 2.50	459.5	457.4	465.1	462.9	57.9: 42.1
	x = 5.00	459.4	457.1	465.0	462.7	63.8: 36.2
		P_1 Cu $2p_{3/2}$ (Cu^{2+})	P_2 Cu $2p_{3/2}$ (Cu^{+})	P_1 Satellite (Cu^{2+})	P_2 Satellite (Cu^{+})	Cu^{2+}: Cu^{+} ratio (%)
Cu $2p_{3/2}$	x = 0.00	934.0	932.0	942.8	940.0	57.1: 42.9
	x = 0.02	–	–	–	–	–
	x = 0.05	934.9	932.5	941.8	944.2	51.1: 48.9
	x = 0.10	934.6	932.4	941.6	944.1	51.4: 48.6
	x = 2.50	934.8	932.6	941.0	943.0	39.5: 60.5
	x = 5.00	934.6	932.6	941.4	943.9	48.2: 51.8
		P_1 W $4d_{5/2}$ (W^{6+})	P_2 W $4d_{5/2}$ (W^{5+})			W^{6+}: W^{5+} ratio (%)
W$4d_{5/2}$	x = 0.00	–	–	–	–	–
	x = 0.02	–	–	–	–	–
	x = 0.05	249.3	246.8	–	–	44.8: 55.2
	x = 0.10	248.8	246.3	–	–	45.3: 54.7
	x = 2.50	248.9	246.5	–	–	42.8: 57.2
	x = 5.00	248.9	246.4	–	–	48.48: 51.2

Fig. 4. (a) Raman spectra of the system $CaCu_3Ti_4O_{12}$: x% W obtained at room temperature for all samples (x = 0.00−5.00). The insets indicate (b) CCTO and (c) $CaWO_4$ lattice deformation with the increase in tungsten content.

wavenumbers (Fig. 4c), indicating that the incorporation of Cu ions at the Ca sites in the $CaWO_4$ structure leads to lattice contraction, which corroborates the Rietveld analysis (Table 2 and Fig. 2b). At 612 cm^{-1}, the weak mode P_8 associated with TiO_2 [83] corroborates the Rietveld refinement results, indicating low TiO_2 content in the composites. Table 4 summarizes each of the vibrational modes used, which characterize the structure of $CaCu_3Ti_4O_{12}$: x% W systems.

Fig. 5 (a) shows the XANES spectra measured at the Ti K-edge for the ceramic powders of the $CaCu_3Ti_4O_{12}$: x% W system. The inset in Fig. 5 (a) shows the occurrence of pre-edge structures (A, B, and C),

which reveal important information on the local symmetry of the octahedrally coordinated titanium ions. Vendrinskii et al. [85] associated low-intensity pre-edge peaks with centrosymmetric crystals. In the CCTO structure, the pre-edge structures indicate the octahedral coordination of the Ti ions within the crystal structure (TiO_6), corroborating the Raman and XRPD results [70,86]. The structures observed in the pre-edge region are the result of two main effects: (1) quadrupole transition between states 1s (occupied) and 3d (unoccupied) titanium; (2) dipolar transition relocated between states 1s (occupied) and 3d (unoccupied) of titanium atoms in neighboring sites. It is essential to consider that

Table 4
Raman modes of the system $CaCu_3Ti_4O_{12}$: x% W.

$CaCu_3Ti_4O_{12}$	Mode	Motion description	Observed wave number (cm^{-1})
	$F_g(1)$	TiO_6 rotation	286
	$F_g(2)$	TiO_6 rotation	401
	$A_g(1)$	TiO_6 rotation	445
	$A_g(2)$	TiO_6 rotation	509
	$E_g(2)$	TiO_6 rotation	509
	$F_g(3)$	$O-Ti-O$ antisymmetric stretching	572
$CaWO_4$	$A_g(2) + B_g(3)$	WO_4^{2-} bending	333
			778
	$B_g(5)$	$O-W-O$ antisymmetric stretching	838
	$A_g(3)$	$W-O$ symmetric stretching	909
TiO_2	$A_g(1)$	$O-Ti-O$ stretching	612

these electronic transitions, generally forbidden for transition metals, become possible due to the overlapping p states of oxygen ions that coordinate titanium ions with unoccupied d states [87]. These pre-peaks are generated when 1s state electrons are excited between the t_{2g} and e_g bands of the octahedral field. Peak A (4968 eV) originates from the combination of the excitonic mechanism from the potential 1s and quadrupole transitions $1s \rightarrow 3d$ (absorption by the octahedral t_{2g} band). These forbidden transitions indicate an electronic arrangement characterized by the hybridization between titanium d states the p states of the surrounding oxygen ions [66,70]. Peak B (4971 eV) is indicative of both dipolar transitions to p states associated with quadrupole $1s \rightarrow 3d$ transitions (absorption by the octahedral e_g band). Peak C (4974 eV) originates mainly from dipolar excitations between the electrons of Ti 1s layers and the t_{2g} states and, for example, from adjacent TiO_6 octahedrons [87−89].

The structure of $CaCu_3Ti_4O_{12}$: x% W provides an ideal coordination geometry for the Jahn-Teller active Cu^{2+} ion [4,70]. Combined with the oxidative properties of tungsten, one would expect copper and titanium ions to change their oxidation states ($Cu^{2+} \rightarrow Cu^+$ and $Ti^{4+} \rightarrow Ti^{3+}$, respectively) with increasing tungsten content [70], as confirmed using the XPS analysis. Additionally, the intensity of peak B remains constant on all samples, independently of tungsten content, indicating that the addition of the W ion does not affect the centrosymmetric character of the TiO_6 octahedra even with partial substitution of W ions at Ti sites. The area under the B peaks can be attributed to the concentration of TiO_5 clusters (TiO_6 octahedra bound by vertices and edges), which can be associated with the octahedral distortion, and are critical to PL emission [86−89]. Fig. 5 (b) exhibits the first oscillations immediately after the edge region (4985−5010 eV) for all samples (x = 0.00−5.00). When dealing with disordered materials, two effects must be considered: (1) variation in edge position (E_0) due to the difference in the vicinity of the absorbing ions; and (2) Debye-Waller effect. In our case, the broadening of the Extended X-ray absorption fine structure (EXAFS) oscillations is combined with a significant magnitude reduction indicates the loss of periodicity in the medium-range structure with increasing tungsten content.

Fig. 5 (c) shows the k^3-weighted EXAFS function $\chi(k)$ vs. k plot for all samples of the ceramic powders of the system $CaCu_3Ti_4O_{12}$: x % W. The magnitude of the Fourier transforms (FT) of $\chi(k)$ in R-space obtained from k^3-weighted $\chi(k)$ is presented in Fig. 5 (d). In order to determine the distance between different ions in the structure, one can use the FT of the EXAFS function considering distinct scattering contributions. Based on a single scattering model, the first peak in the FT spectra is associated with the scattering of photoelectrons by near neighbors present in the first shell. In this case, the Ti−O bond distance was found to be 1.50 Å (first shell), which is related to oxygen atoms arranged octahedrally around the Ti ions. The second shell peak was associated to Ca/Cu

neighbors (Ti−Ca/Cu bond distance 2.72 Å), and the third ones to Ti neighbors (Ti−Ti bond distance 4.74 Å). It is possible to observe that the Ti−O distance slightly increases with the increase in W content. This result can be associated with the incorporation of tungsten ions ($R_{W^{6+}} = 0.600$ Å and $R_{W^{5+}} = 0.620$ Å) at the titanium sites ($R_{Ti^{4+}} = 0.605$ Å) and to the reduction of titanium ($R_{Ti^{3+}} = 0.670$ Å; $R_{Ti^{4+}} = 0.605$ Å) and copper ions ($R_{Cu^+} = 0.600$ Å; $R_{Cu^{2+}} = 0.570$ Å), in agreement with the Raman, Rietveld refinement and XPS results, which indicate the lattice expansion with the addition of W ions, corroborating both the Rietveld analysis and XANES measurements. Furthermore, lattice deformation may also associated with the increase in the local charge/electronegativity (EN) caused by the partial substitution of Ti^{3+}/Ti^{4+} ions (EN = 1.73) by W^{5+}/W^{6+} ions (EN = 2.17) [90]. Thus, the initial hypothesis that tungsten ions added are partially incorporated into titanium sites is supported by both EXAFS and Rietveld refinement. The higher intensity of the second Ti−Ti shell (5.66 Å) evidences the higher mean coordination number of Ti at the second cationic coordination shell. Table 5 presents the best fitting results of EXAFS spectra for all samples (x = 0.00−5.00) performed based on the structural parameters obtained from the ICSD #259849.
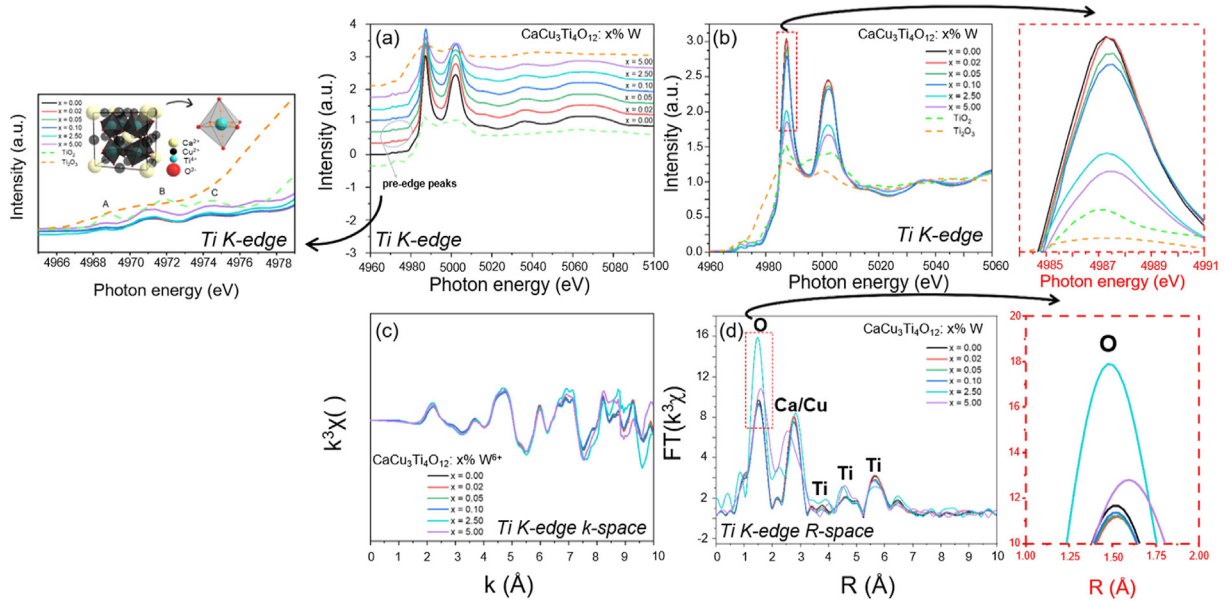
Fig. 6(a−f) depicts FEG-SEM micrographs with the particle size distribution (insets) of the ceramic system $CaCu_3Ti_4O_{12}$: x% W (x = 0.00−5.00). All samples revealed a mono-dispersed distribution of submicrometric particles. Initially, for low tungsten content samples (x = 0.00−0.10), spherical-like particles are observed with some degree of agglomeration as a result of energy minimization. Further incorporation of W ions (x = 2.50−5.00) reveals a tendency of the particles to grow as faceted particles due to changing surface energies, as the local chemistry is changed. Such effect is also observed on CCTO powders synthesized by the molten salt method in the presence of alkaline-metal ions (Li$^+$, Na$^+$, K$^+$), due to high mobility and strong electrostatic interaction between the ions with the surface. Highly oriented face crystals originate from low energy surfaces, which leads to slow crystal growth [41,91].

3.2. Computational methods

Aspects related to the occupancy of the added W ions, Ti/Cu reduction, and the formation of charge-compensating defects have a direct impact on the optical properties of CCTO based ceramics. Thus, the most energetically favorable occupancy schemes were elucidated, and the values were estimated quantitatively by our calculations.

First, static simulations were performed to verify in which site the tungsten ions were incorporated into the $CaCu_3Ti_4O_{12}$ structure. Fig. 7 shows the solution energy for each possible defect reaction considered, which was calculated following the procedure reported in previous works [92−95]. All defect reactions, written according to the Kröger-Vink notation, are shown in Table 6. The

Fig. 5. XAS measurements for the system $CaCu_3Ti_4O_{12}$: x% W^{6+} performed at room temperature. (a) shows the XANES spectra. The insets highlight the pre-edge peaks. (b) XANES spectra (the inset highlights the first oscillation after the absorption edge), (c) Ti K − edge EXAFS function, χ (k) k^3-weighted in k-space, and (d) Fourier transforms of χ (k) in R-space (the change in intensity of the first shell (Ti−O) peaks is highlighted in the inset).
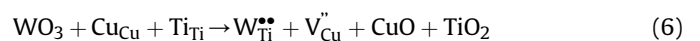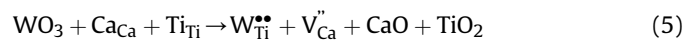
Table 5
EXAFS fitting parameters for all samples of the system $CaCu_3Ti_4O_{12}$: x% W (x = 0.00−5.00).

Samples	R-factor	N_{ind}/k-range	N_{var}/R-range	χ^2/χ^2_v	Path	CN	R (A)	σ^2 ($Å^2$)	ΔE (eV)
x = 0.00	0.023	31.11/2.0−11.0	20/1−6.5	1200.39/107.99	Ti − O	6	1.48 ± 0.02	0.005 ± 0.001	4.43 ± 1.21
					Ti − Ca	2	2.81 ± 0.08	0.002 ± 0.007	4.43 ± 1.21
					Ti − Cu	6	2.71 ± 0.01	0.011 ± 0.007	4.43 ± 1.21
					Ti − Ti	6	3.29 ± 0.07	0.003 ± 0.004	4.43 ± 1.21
x = 0.02	0.025	31.11/2.0−11.0	20/1−6.5	1268.11/114.09	Ti − O	6	1.48 ± 0.02	0.006 ± 0.001	4.03 ± 1.27
					Ti − Ca	2	2.80 ± 0.07	0.0003 ± 0.004	4.03 ± 1.27
					Ti − Cu	6	2.72 ± 0.003	0.014 ± 0.009	4.03 ± 1.27
					Ti − Ti	6	3.30 ± 0.08	0.003 ± 0.004	4.03 ± 1.27
x = 0.05	0.023	31.11/2.0−11.0	20/1−6.5	745.60/67.08	Ti − O	6	1.48 ± 0.02	0.006 ± 0.001	3.81 ± 1.22
					Ti − Ca	2	2.80 ± 0.08	0.0004 ± 0.003	3.81 ± 1.22
					Ti − Cu	6	2.71 ± 0.01	0.014 ± 0.009	3.81 ± 1.22
					Ti − Ti	6	3.30 ± 0.09	0.003 ± 0.004	3.81 ± 1.22
x = 0.10	0.021	31.11/2.0−11.0	20/1−6.5	1348.67/121.34	Ti − O	6	1.48 ± 0.02	0.006 ± 0.001	3.99 ± 1.17
					Ti − Ca	2	2.79 ± 0.08	0.0004 ± 0.003	3.99 ± 1.17
					Ti − Cu	6	2.73 ± 0.01	0.015 ± 0.009	3.99 ± 1.17
					Ti − Ti	6	3.29 ± 0.09	0.004 ± 0.004	3.99 ± 1.17
x = 2.50	0.042	25.21/2.5−9.8	14/1−6.5	732.00/65.33	Ti − O	6	1.46 ± 0.04	0.001 ± 0.001	4.55 ± 1.92
					Ti − Ca	2	2.81 ± 0.13	0.001 ± 0.003	4.55 ± 1.92
					Ti − Cu	6	2.70 ± 0.03	0.010 ± 0.008	4.55 ± 1.92
					Ti − Ti	6	3.31 ± 0.09	0.016 ± 0.007	4.55 ± 1.92
x = 5.00	0.15	26.25/2.0−9.6	14/1−6.5	3085.87/251.95	Ti − O	6	1.49 ± 0.01	0.010 ± 0.010	4.74 ± 2.94
					Ti − Ca	2	2.93 ± 0.20	0.001 ± 0.003	4.74 ± 2.94
					Ti − Cu	6	2.68 ± 0.04	0.007 ± 0.002	4.74 ± 2.94
					Ti − Ti	6	3.31 ± 0.09	0.017 ± 0.008	4.74 ± 2.94

preferred mechanism can be inferred by comparing the corresponding solution energies, defined as the sum of each basic defect formation energy (vacancies and interstitials) normalized by the numbers of defects. The solution energy for the incorporation of W ions into Ca and Cu is much higher than the solution energy for incorporation at Ti sites. Thus, according to our calculations, W ions are most likely to be incorporated into the CCTO structure in Ti sites generating Ca vacancies (charge compensator# 13, Table 6). Additionally, it should be noted that the solution energy for W substitution at the Ti site compensated by Cu vacancies (reaction 14, Table 6), and by Cu antisite (charge compensator# 16, Table 6) are close to the solution energy for charge compensator# 13. This small
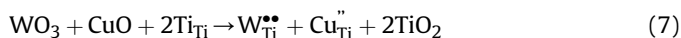
difference implies a chance of both defects occurring as charge compensation for this incorporation.

Based on the XRPD results, and the simulations, the evolution of the structure in the ceramic system $CaCu_3Ti_4O_{12}$: x% W can be thought of as in terms of Kröger-Vink reactions (Eq. (5)−7):

$$WO_3 + Ca_{Ca} + Ti_{Ti} \rightarrow W_{Ti}^{\bullet\bullet} + V_{Ca}^{''} + CaO + TiO_2 \quad (5)$$

$$WO_3 + Cu_{Cu} + Ti_{Ti} \rightarrow W_{Ti}^{\bullet\bullet} + V_{Cu}^{''} + CuO + TiO_2 \quad (6)$$

Fig. 6. FEG-SEM micrographs and particle size distribution of the system $CaCu_3Ti_4O_{12}$: x% W for samples (a) x = 0.00, (b) x = 0.02, (c) x = 0.05, (d) x = 0.10, (e) x = 2.50, and (f) x = 5.00.). The insets show the particle size distribution for each of the samples.

$$WO_3 + CuO + 2Ti_{Ti} \rightarrow W_{Ti}^{\bullet\bullet} + Cu_{Ti}'' + 2TiO_2 \tag{7}$$

where the formation of the CTO phase on samples x = 0.05−0.10 results from a reduction on the Cu: Ca ratio in the CCTO structure [96,97]. Likewise, on samples x = 2.50−5.00, the formation of calcium tungstate ($CaWO_4$) indicates that the tungsten ions exceeded the solubility limit in the CCTO structure. The XRD results also show the presence of the phase CuO in samples x = 0.05−0.10, which suggests that the incorporation of tungsten ions be compensated by copper and calcium vacancies (V_{Cu}'' and V_{Ca}''), as shown in Eqs. (5) and (6), corroborating the simulations.

3.3. Optical characterization

Fig. 8(a−f) presents the ultraviolet−visible (UV−Vis) spectra collected at room temperature in diffuse reflectance mode for the ceramic powders of the system $CaCu_3Ti_4O_{12}$: x% W. The Kubelka-Munk mathematical model (Eq. (2)) was applied to obtain the $(\alpha h\nu)^2$ vs. E curves. All samples behaved as expected for a $CaCu_3Ti_4O_{12}$ system with perovskite cubic structure (2.21 < E_{gap} < 2.29), which is consistent with the high percentage of CCTO phase identified by means of the Rietveld analysis [28]. The optical bandgap results indicate an electronic structure in which the upper region of

the valence band (VB) and the lower region of the conduction band (CB) are composed of O(2p) − Cu(3d) and O(2p) − Ti(3d) hybridized states, respectively [27,88]. Furthermore, the optical bandgap energy of samples x = 0.02 and x = 0.05 increase in comparison with sample x = 0.00, indicating a more insulating system, which is associated with higher W content. However, the incorporation of W ions at the Ti sites leads to charge recombination and the formation of metal vacancies and, thus, to a decrease in the optical bandgap energy on sample x = 0.10. With $Ca_{1-x}Cu_xWO_4$ formation, the number of negative charges available decreases, improving the insulating character as noted for samples x = 2.50 and x = 5.00, in accordance with the structural and theoretical analysis previously presented.

The Absorbance vs. wavelength curve for the ceramic powders of the system $CaCu_3Ti_4O_{12}$: x% W is shown in Fig. 8 (g). All samples exhibit two absorption bands with different intensity, which is typical for the CCTO phase with a perovskite cubic structure with space group *Im-3*. In the low energy side of the spectrum, the lower intensity band is associated with Cu D-state transitions. It is worth noting that in samples x = 2.50 and 5.00, the tail linking the two absorption bands are slightly shifted in comparison to the other samples. This result indicates the presence of deep-level defect states within the bandgap region of the material. Additionally, the presence of two absorption bands in the absorbance spectra of
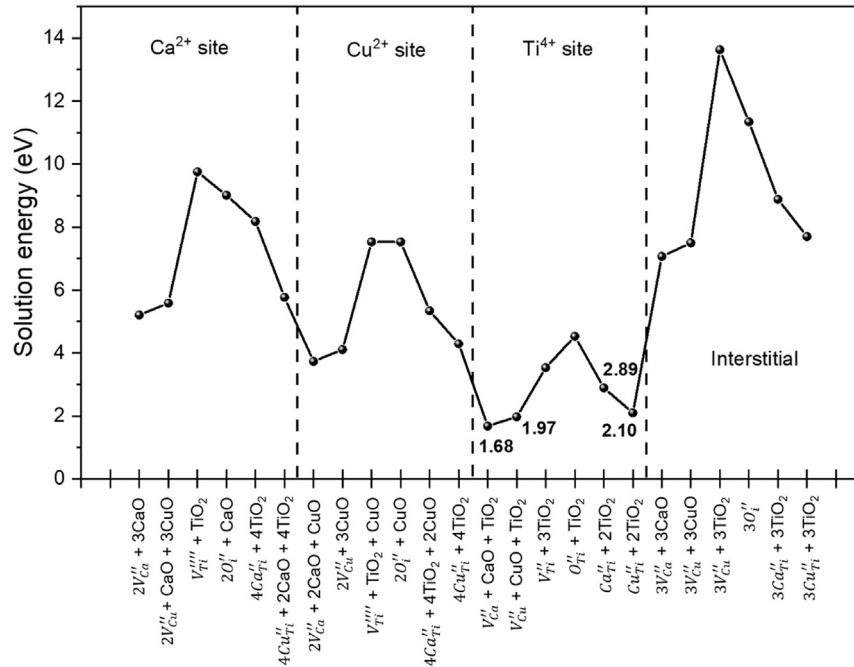
Fig. 7. Solution energies for the incorporation of W ions at Ca, Cu, Ti, and interstitial sites in the structure of CCTO.
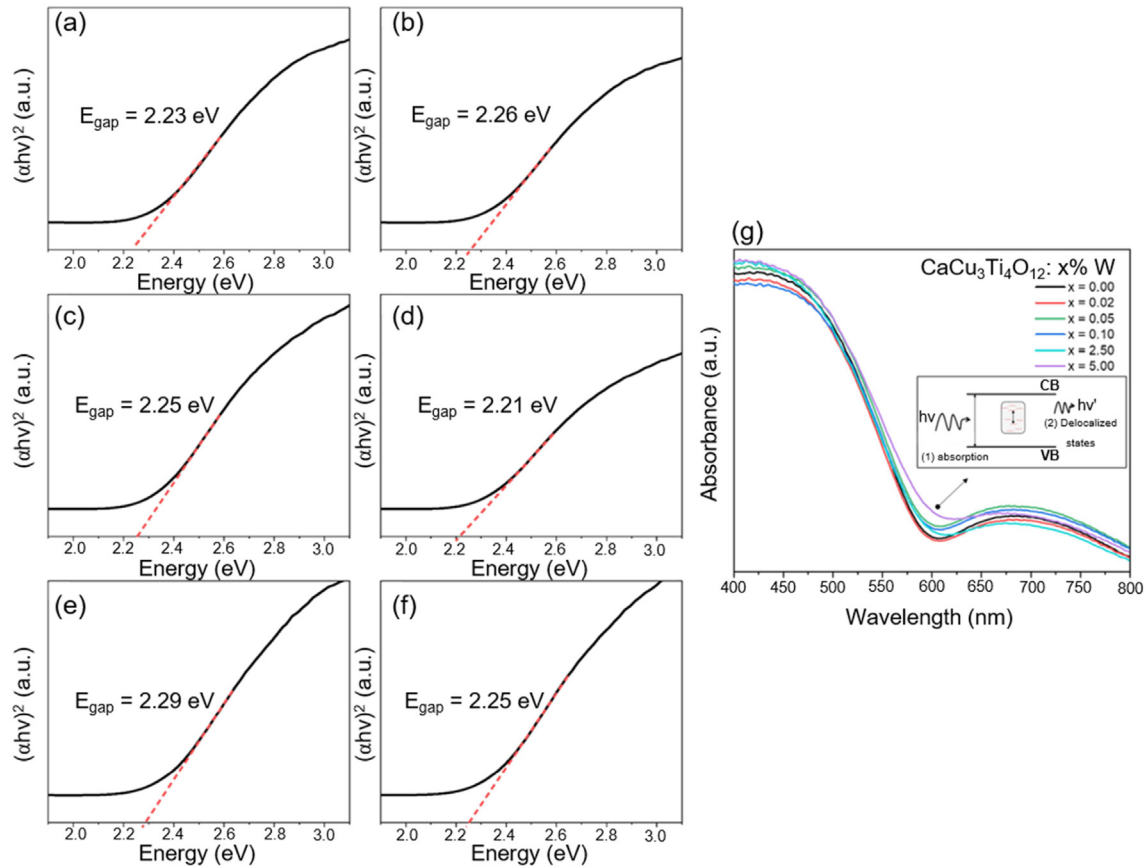
Table 6
Kröger-Vink reactions considered for the incorporation of W ions in the $CaCu_3Ti_4O_{12}$ structure on the theoretical simulations.

Site	Charge compensation	Reaction	Solution Energy (eV)
Ca	1. Ca vacancy	$WO_3 + 3Ca_{Ca} \rightarrow W_{Ca}^{\bullet\bullet\bullet\bullet} + 2V_{Ca}'' + 3CaO$	5.21
	2. Cu vacancy	$WO_3 + Ca_{Ca} + 2Cu_{Cu} \rightarrow W_{Ca}^{\bullet\bullet\bullet\bullet} + 2V_{Cu}'' + CaO + 2CuO$	5.59
	3. Ti vacancy	$WO_3 + Ti_{Ti} + Ca_{Ca} \rightarrow W_{Ca}^{\bullet\bullet\bullet\bullet} + V_{Ti}'''' + TiO_2 + CaO$	9.75
	4. O interstitial	$WO_3 + Ca_{Ca} \rightarrow W_{Ca}^{\bullet\bullet\bullet\bullet} + 2O_i'' + CaO$	9.01
	5. Antisite Ca_{Ti}''	$2WO_3 + 2CaO + 2Ca_{Ca} \rightarrow 2W_{Ca}^{\bullet\bullet\bullet\bullet} + 4Ca_{Ti}'' + 4TiO_2$	8.18
	6. Antisite Cu_{Ti}''	$2WO_3 + 4CuO + 2Ca_{Ca} + 4Ti_{Ti} \rightarrow 2W_{Ca}^{\bullet\bullet\bullet\bullet} + 4Cu_{Ti}'' + 2CaO + 4TiO_2$	5.77
Cu	7. Ca vacancy	$WO_3 + 2Ca_{Ca} + Cu_{Cu} \rightarrow W_{Cu}^{\bullet\bullet\bullet\bullet} + 2V_{Ca}'' + 2CaO + CuO$	3.73
	8. Cu vacancy	$WO_3 + 3Cu_{Cu} \rightarrow W_{Cu}^{\bullet\bullet\bullet\bullet} + 2V_{Cu}'' + 3CuO$	4.11
	9. Ti vacancy	$WO_3 + Ti_{Ti} + Cu_{Cu} \rightarrow W_{Cu}^{\bullet\bullet\bullet\bullet} + V_{Ti}'''' + TiO_2 + CuO$	7.53
	10. O interstitial	$WO_3 + Cu_{Cu} \rightarrow W_{Cu}^{\bullet\bullet\bullet\bullet} + 2O_i'' + CuO$	7.53
	11. Antisite Ca_{Ti}''	$2WO_3 + 4CaO + 2Cu_{Cu} + 4Ti_{Ti} \rightarrow 2W_{Cu}^{\bullet\bullet\bullet\bullet} + 4Ca_{Ti}'' + 2CuO + 4TiO_2$	5.34
	12. Antisite Cu_{Ti}''	$2WO_3 + 2CuO + 2Cu_{Cu} \rightarrow 2W_{Cu}^{\bullet\bullet\bullet\bullet} + 4Cu_{Ti}'' + 4TiO_2$	4.29
Ti	13. Ca vacancy	$WO_3 + Ca_{Ca} + Ti_{Ti} \rightarrow W_{Ti}^{\bullet\bullet} + V_{Ca}'' + CaO + TiO_2$	1.68
	14. Cu vacancy	$WO_3 + Cu_{Cu} + Ti_{Ti} \rightarrow W_{Ti}^{\bullet\bullet} + V_{Cu}'' + CuO + TiO_2$	1.97
	15. Ti vacancy	$2WO_3 + 3Ti_{Ti} \rightarrow 2W_{Ti}^{\bullet\bullet} + V_{Ti}'''' + 3TiO_2$	3.53
	16. O interstitial	$WO_3 + Ti_{Ti} \rightarrow W_{Ti}^{\bullet\bullet} + O_i'' + TiO_2$	4.53
	17. Antisite Ca_{Ti}''	$WO_3 + CaO + 2Ti_{Ti} \rightarrow W_{Ti}^{\bullet\bullet} + Ca_{Ti}'' + 2TiO_2$	2.89
	18. Antisite Cu_{Ti}''	$WO_3 + CuO + 2Ti_{Ti} \rightarrow W_{Ti}^{\bullet\bullet} + Cu_{Ti}'' + 2TiO_2$	2.10
$W_i^{\bullet\bullet\bullet\bullet\bullet\bullet}$	19. Ca vacancy	$WO_3 + 3Ca_{Ca} \rightarrow W_i^{\bullet\bullet\bullet\bullet\bullet\bullet} + 3V_{Ca}'' + 3CaO$	7.07
	20. Cu vacancy	$WO_3 + 3Cu_{Cu} \rightarrow W_i^{\bullet\bullet\bullet\bullet\bullet\bullet} + 3V_{Cu}'' + 3CuO$	7.50
	21. Ti vacancy	$2WO_3 + 3Ti_{Ti} \rightarrow 2W_i^{\bullet\bullet\bullet\bullet\bullet\bullet} + 3V_{Ti}'''' + 3TiO_2$	13.63
	22. O interstitial	$WO_3 \rightarrow W_i^{\bullet\bullet\bullet\bullet\bullet\bullet} + 3O_i''$	11.34
	23. Antisite Ca_{Ti}''	$WO_3 + 3CaO \rightarrow W_i^{\bullet\bullet\bullet\bullet\bullet\bullet} + 3Ca_{Ti}'' + 3TiO_2$	8.88
	24. Antisite Cu_{Ti}''	$WO_3 + 3CuO \rightarrow W_i^{\bullet\bullet\bullet\bullet\bullet\bullet} + 3Cu_{Ti}'' + 3TiO_2$	7.70

CCTO, both in the visible-light region, corroborates the occurrence of cationic species in distinct sites within the highly distorted perovskite structure of CCTO, which is in accordance with the XRD, Raman, and XAS results.

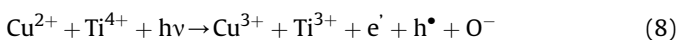Fig. 9(a−f) shows the deconvolution PL spectra for all samples of the system $CaCu_3Ti_4O_{12}$: x% W (x = 0.00−5.00) excited by a 250 nm wavelength light. Sample x = 0.00 revealed an orange-red emission (577 nm−622 nm), which is associated with deep-level defects, such as electrons (e') and holes ($h^\bullet$) induced by the excitation source in the optical bandgap region. With the incorporation of W ions at the Ti sites, the PL emissions of samples x = 0.02−2.50 shifted towards a violet-blue-green (455 nm−492 nm), which is

Fig. 8. UV–vis spectra and of the system $CaCu_3Ti_4O_{12}$: x% W obtained at room temperature for samples (a) x = 0.00, (b) x = 0.02, (c) x = 0.05, (d) x = 0.10, (e) x = 2.50, and (f) x = 5.00. The inset (g) shows the absorbance spectra of the system $CaCu_3Ti_4O_{12}$: x% W obtained at room temperature for all samples (x = 0.00–5.00).

due to the formation of shallow defects, near the valence (VB) and/ or conduction (CB) bands [98,99]. Additionally, green luminescence (492 nm–577 nm), is associated with self-trapped/recombination of charges, and also to particle size. The increase in green emission for samples x = 0.02, 0.05, and 2.50 in comparison to sample x = 0.00 is a result of charge recombination processes occurring between opposite charge defects in the bandgap region due to electrostatic imbalances. The orange-red emissions can be associated with the deep-level defects located in the optical bandgap region, and the emission can be associated with the radiative recombination of a photogenerated hole with an electron occupying the $V_O^\bullet$ [34,100,101]. Based on these results, the origin of the PL response in the ceramic powders of the system $CaCu_3Ti_4O_{12}$: x% W can be described in terms of the charge transfer between complex clusters ($[TiO_5V_O^\bullet]$, $[WO_5V_O^\bullet]$, $[CaO_{11}V_O^\bullet]$, and $[CuO_{11}V_O^\bullet]$), and TiO_6, CaO_{12}, and CuO_{12}, which are affected by structural distortions and point defects (e.g., oxygen and metal vacancies). Additionally, the PL response in samples with x = 2.50 and 5.00 is affected by the presence of $CaWO_4$, which has a bandgap comparable to that of CCTO, leading to a highly efficient intrinsic luminescence.

Thus, the visible light is capable of inducing electron-hole polarons as a result of the charge transfer between adjacent ions (Eq. (8)).

$$Cu^{2+} + Ti^{4+} + h\nu \rightarrow Cu^{3+} + Ti^{3+} + e^{'} + h^\bullet + O^- \qquad (8)$$

where $h\nu$ represents the absorbed energy ($h\nu \geq E_{gap}$), $\boldsymbol{e}^{'}$ the electrons, and $\boldsymbol{h}^\bullet$ the holes.

Fig. 10 shows the PL radiant efficiency (RE) as a function of tungsten content for all samples of the system $CaCu_3Ti_4O_{12}$: x% W (x = 0.00–5.00). For samples x = 0.02, 0.05, 0.10, and 5.00, the results show an increase in the radiant efficiency to approximately 20% with the addition of W ions to the CCTO structure when compared to sample x = 0.00 (η_r 10.9%), possibly related to the electrochromic nature of tungsten, and the formation of intermediary level defects within the optical bandgap region of CCTO as a result of the incorporation of W ions at the Ti sites. On sample x = 2.50, the RE value increases significantly (η_r 55.2%) when compared to sample x = 0.00 (η_r 10.9%), which can be associated with the efficient recombination between opposite charge defects, namely metal vacancies ($V_{Ca}^{''}$, $V_{Cu}^{''}$) and holes ($\boldsymbol{h}^\bullet$) as well as to electron-hole recombination [102].

3.4. General discussion

Based on both the theoretical simulations and experimental data (structural and optical measurements), we proposed a practical model to explain how the PL emissions of the system $CaCu_3Ti_4O_{12}$: x% W are influenced by the presence of shallow and/or deep-level defects in the electronic structure. Fig. 11 illustrates the mechanism responsible for generating the specific PL emission for each of the samples (x = 0.00–5.00) and the associated coordinate in the chromaticity diagram (CIE – *Commission internationale de l'eclairage* 1931) using a 250 nm wavelength light as the excitation source. The CIE chromaticity diagram evidenced two groups of samples: x = 0.00, 0.10, and 5.00 emit on the red; while samples x = 0.02, 0.05, and 2.50 are blue-emitters, which is associated with the combination of different types of defects in the bandgap region
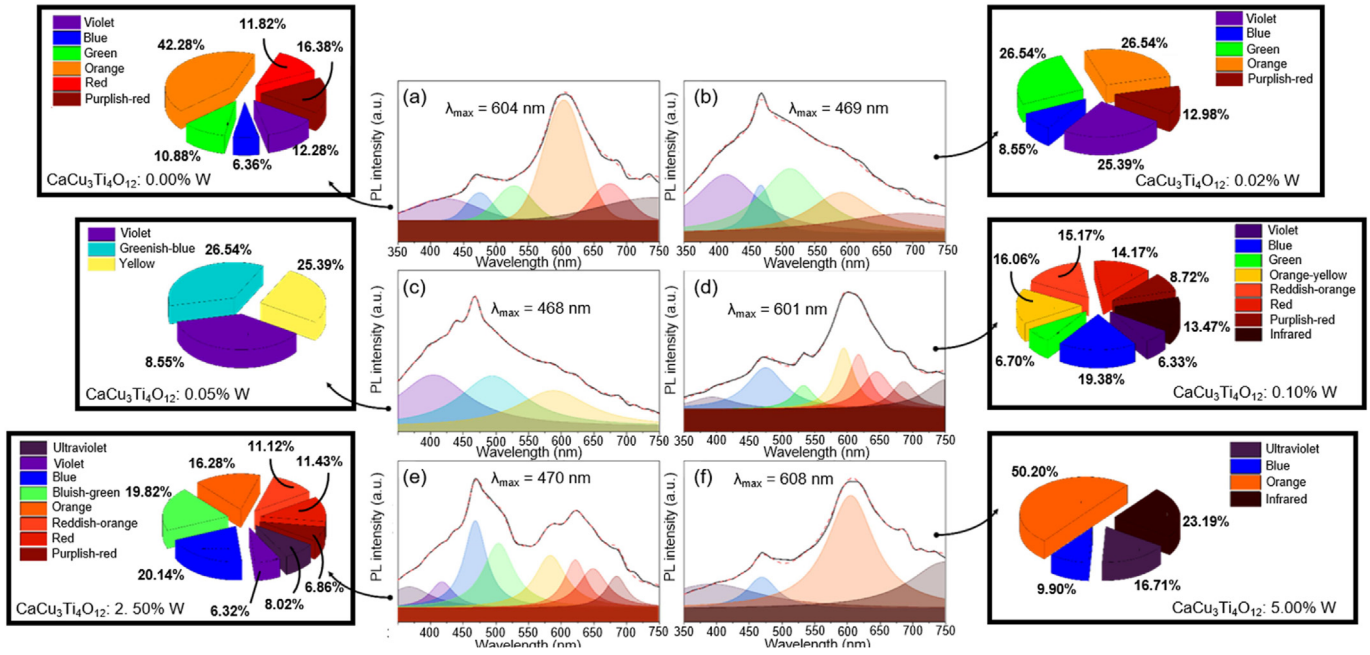
Fig. 9. Deconvolution of the PL spectrum of the system CaCu$_3$Ti$_4$O$_{12}$: x% W^{6+} obtained at room temperature for samples (a) x = 0.00, (b) x = 0.02, (c) x = 0.05, (d) x = 0.10, (e) x = 2.50, and (f) x = 5.00.
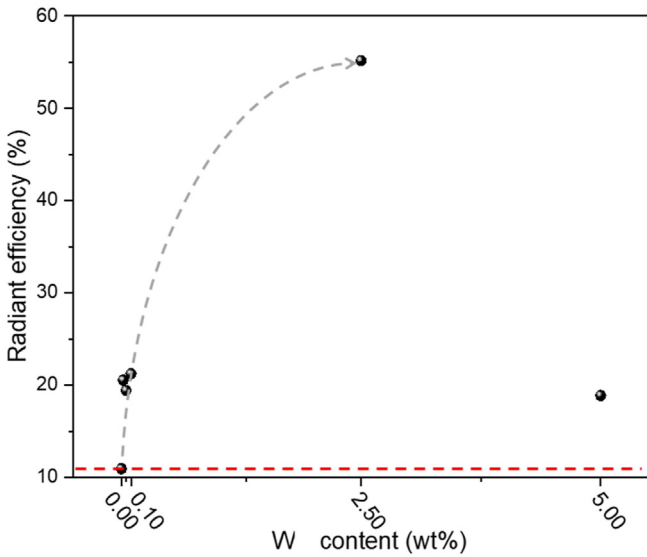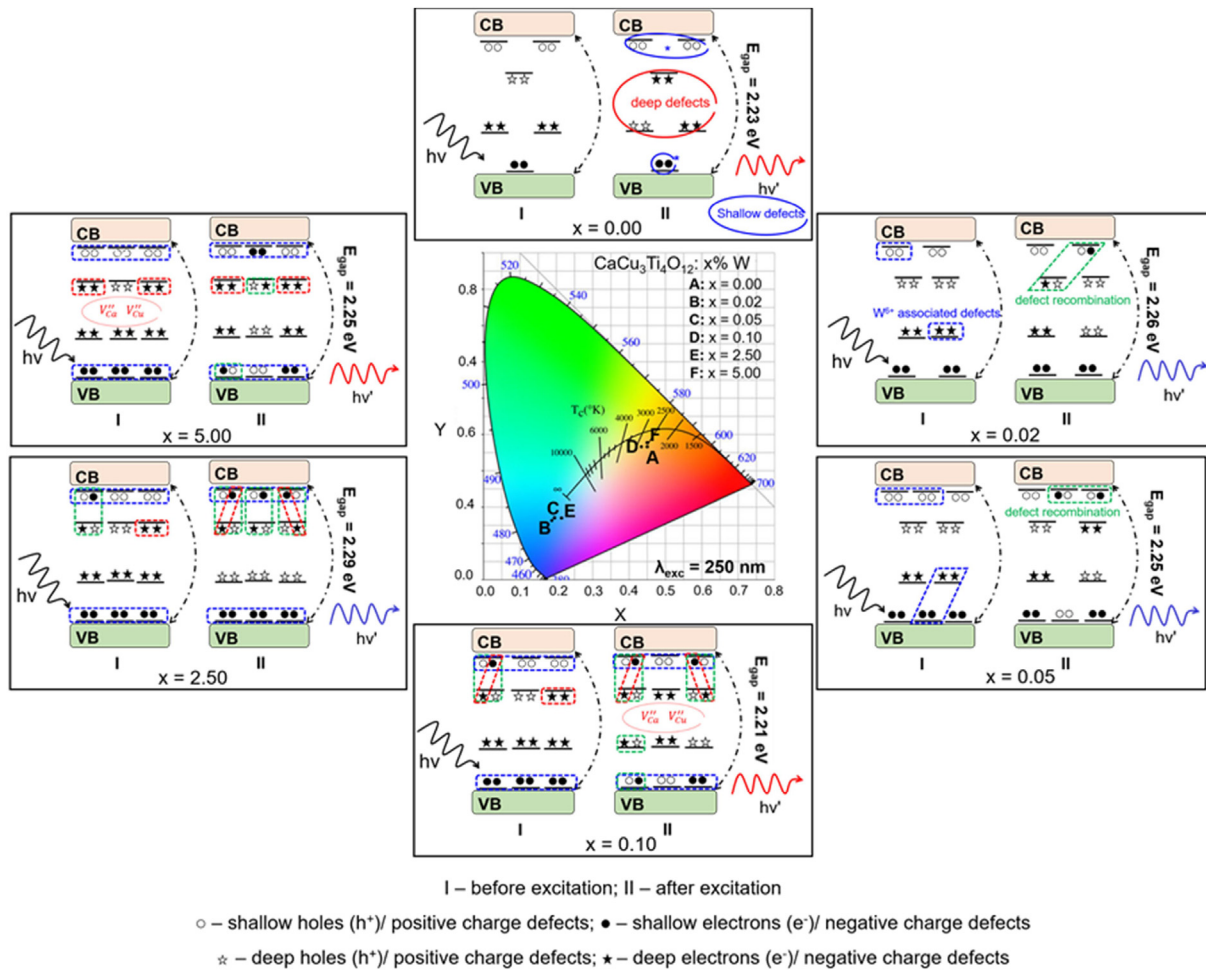

Fig. 10. Radiant efficiency vs. W content for all samples of the system CaCu$_3$Ti$_4$O$_{12}$: W (x = 0.00−5.00).

of the system CaCu$_3$Ti$_4$O$_{12}$: x% W. Furthermore, one can observe that the coordinates of the samples (A, B, C, D, E, and F) in the CIE diagram are relatively distant from the edges, which indicates the contribution of different color centers in the emission range. Therefore, the proposed model was based on the formation of different types of defects (*e'*, *h*•V_{Ca}'', and V_{Cu}'') induced within the bandgap region by both the addition of W ions and the excitation light source. Shallow (spheres) and deep-level (stars) defects produce different PL emissions. The charge recombination between opposite charge defects also contributes to the emissions and must be taken into account. Furthermore, the theoretical simulations revealed the presence of oxygen and metal vacancies (V_{Ca}''/ V_{Cu}''), and

local symmetry disruption with increasing tungsten content, which was confirmed by the experimental (Raman and XAS data) results. The formation of oxygen vacancies is enhanced by the addition of tungsten ions in the CCTO system, which induces reduction of copper and titanium ions (Cu^{2+}→Cu$^+$ and Ti^{4+}→Ti^{3+}, respectively), as confirmed by the XPS results. The chromaticity diagram also provides information on the correlated color temperature (CCT) of materials. The CCT, measured in Kelvin, is useful for characterizing the white light emitted. Our results show that samples with x = 0.00, 0.10, and 5.00 emit in the "ultra-warm" white region (2246 K, 2543 K, and 2342 K, respectively), which is characteristic of an incandescent light bulb emission. On the other hand, samples with x = 0.02, 0.05, and 2.50 emit in the "cool white" region (7687 K, 6150 K, and 7672 K, respectively) characteristic of daylight, or an RGB monitor reference white point [103,104].

The PL results show the occurrence of emissions associated with the direct transition from of electrons from the valence to the conduction band (VB-CB). Additionally, when excited by light of specific wavelength (e.g., 250 nm), the result is the formation of defect levels (*e'* and *h*•) in the bandgap of CCTO. On sample x = 0.00, the red emission can be justified by the formation of a higher concentration of deep defects in comparison to shallow defects. The addition of W ions to the CCTO structure on all samples x = 0.02−0.05 leads to the formation of shallow defects near the VB and/or the CB, which is related to the blue emissions [105]. On samples x = 0.02−0.05, the green emissions are associated with charge recombination of opposite charge defects, such as electron-hole recombination. Furthermore, the presence of TiO$_2$ on sample x = 0.05 with intrinsic green PL emission contributes to producing different tones of blue PL emissions on samples x = 0.02 and 0.05. On sample x = 0.10, the red PL emissions are associated with the formation of metal vacancies (V_{Ca}'' and V_{Cu}''), generating deep-level defects in the bandgap region. This sort of defect, often referred to as traps, are known to increase the electron-hole recombination [106,107], producing some extent of green emission, which can also be associated with TiO$_2$ intrinsic PL emissions. The CaTiO$_3$ phase on

Fig. 11. Proposed models for the electronic structure and PL emission mechanism for the system CaCu₃Ti₄O₁₂: x% W (x = 0.00–5.00), and the associated chromaticity diagram (CIE 1931).

sample x = 0.10 also contributes to the red-orange PL emission due to its intrinsic characteristics [108]. It is important to note that the CaWO₄ phase has an intrinsic PL emission on the blue region and shows a stronger contribution to sample x = 2.50 in comparison to sample x = 5.00 [109]. On sample x = 2.50, defect levels formed by the metal vacancies tend to recombine with holes and, thus, increase the blue-green emission. On sample x = 5.00, on the other hand, the red PL emission is favored due to the higher concentration of deep level defects in the bandgap region. This result corroborates both the theoretical computing simulations and the experimental data (XRPD, Raman, XAS), which show that W ions are incorporated at the Ti sites, generating metal vacancies as charge compensators. Thus, it was possible to modulate the wavelength and intensity of PL emissions of CaCu₃Ti₄O₁₂ by inducing defects in the structure with the addition of W ions.

4. Conclusions

Ceramic powders of the system CaCu₃Ti₄O₁₂: x % W were prepared via nontoxic, low-cost, and simple solid-state reaction. The experimental data confirmed that the W ions added to the CCTO structure are incorporated at the Ti sites, leading to lattice expansion, which was consistent with the theoretical computing simulations. The XPS results confirm the presence of W^{5+}, Ti^{3+}, and Cu^+ ions in all samples of the CaCu₃Ti₄O₁₂: x% W system, leading to

structural changes that strongly influence the PL response of the material. The incorporation of tungsten ions stimulate local disorder within the structure by inducing point defects (V_{Ca}'', V_{Cu}'', and $V_O^{\bullet\bullet}$). Furthermore, the addition of W ions to the system contributed to the generated shallow and deep level defects to the electronic structure of CCTO, producing slight changes in the bandgap energy (E_{gap}). The increase in blue emission is associated with the incorporation of W ions, which form shallow defects. Blue PL emissions on samples x = 0.02 and 0.05 were associated mainly with the occurrence of electron-hole recombinations. On sample 2.50, the blue emission was related to recombination between metal vacancies (V_{Ca}'' and V_{Cu}'') and holes. On the other hand, on samples x = 0.10, and 5.00, red PL emissions were associated with the presence of V_{Ca}'' and V_{Cu}'' generating deep-level defects. Thus, our research shows evidence that CaCu₃Ti₄O₁₂ (CCTO): W ceramic systems may be promising to photonics applications.

CRediT authorship contribution statement

H. Moreno: Conceptualization, Methodology, Writing - original draft. **J.A. Cortés:** Investigation, Writing - review & editing. **F.M. Praxedes:** Writing - review & editing. **S.M. Freitas:** Formal analysis, Writing - review & editing. **M.V.S. Rezende:** Formal analysis, Writing - review & editing. **A.Z. Simões:** Writing - review & editing. **V.C. Teixeira:** Formal analysis, Writing - review & editing,

Supervision. **M.A. Ramirez:** Conceptualization, Methodology, Supervision.

Declaration of competing interest

The authors declare that they have no known competing financial interests or personal relationships that could have appeared to influence the work reported in this paper.

Acknowledgments

Appendix A. Supplementary data

Supplementary data to this article can be found online at https://doi.org/10.1016/j.jallcom.2020.156652.

References

[1] S. Kaur, A. Kumar, A.L. Sharma, D.P. Singh, Dielectric and energy storage behavior of $CaCu_3Ti_4O_{12}$ nanoparticles for capacitor application, Ceram. Int. 45 (2019) 7743—7747.

[2] C. Sripakdee, K. Prompa, E. Swatsitang, T. Putjuso, Very high-performance dielectric and non-ohmic properties of novel X8R type $Ca_{1-1.5x}Ho_xCu_3Ti_4O_{12}/TiO_2$ ceramics, J. Alloys Compd. 779 (2019) 521—530.

[3] K. Prompa, E. Swatsitang, T. Putjuso, Enhancement of nonlinear electrical properties with high performance dielectric properties of $CaCu_{2.95}Cr_{0.05}Ti_{4.1}O_{12}$ ceramics, Ceram. Int. 44 (2018) S72—S75.

[4] P.Y. Raval, A.R. Makadiya, P.R. Pansara, P.U. Sharma, N.H. Vasoya, J.A. Bhalodia, S. Kumar, S.N. Dolia, K.B. Modi, Effect of thermal history on structural, microstructural properties and J — E characteristics of $CaCu_3Ti_4O_{12}$ polycrystalline ceramic, Mater. Chem. Phys. 212 (2018) 343—350.

[5] M. Ahmadipour, N.A. Rejab, M.F. Ab Rahman, M.F. Ain, Z.A. Ahmad, High sensitivity and selectivity of $CaCu_3Ti_4O_{12}$-ZnO composites towards acetone gas at room temperature, Ceram. Int. 44 (2018) 6904—6911.

[6] A. Natkaeo, D. Phokharatkul, J.H. Hodak, A. Wisitsoraat, S.K. Hodak, Highly selective sub—10 ppm H_2S gas sensors based on Ag-doped $CaCu_3Ti_4O_{12}$ films, Sensor. Actuator. B Chem. 260 (2018) 571—580.

[7] M. Li, Study of the humidity-sensing mechanism of $CaCu_3Ti_4O$, Sensor. Actuator. B Chem. 228 (2016) 443—447.

[8] K. Pal, R. Jana, A. Dey, P.P. Ray, M.M. Seikh, A. Gayen, Application of $CaCu_3Ti_4O_{12}$ based quadruple perovskites as a promising candidate for optoelectronic devices, Chem. Phys. Lett. 699 (2018) 229—233.

[9] C.R. Tubío, F. Guitián, A. Gil, Synthesis and characterization of three dimensionally ordered macroporous of $CaCu_3Ti_4O_{12}$ ceramics, Mater. Lett. 190 (2017) 28—32.

[10] K. Pal, R. Jana, A. Dey, P.P. Ray, M.M. Seikh, A. Gayen, Performance analysis of Fe-doped calcium copper titanate quadruple perovskite in optoelectronic device, Chem. Phys. Lett. 709 (2018) 110—115.

[11] M. Moniruddin, B. Ilyassov, X. Zhao, E. Smith, T. Serikov, N. Ibrayev, R. Asmatulu, N. Nuraje, Recent progress on perovskite materials in photovoltaic and water splitting applications, Mater, Today Energy 7 (2018) 246—259.

[12] K. Pal, A. Mondal, R. Jana, P.P. Ray, A. Gayen, Domestic LED light driven methylene blue degradation by $g-C_3N_4-CaCu_3Ti_4O_{12}$ composite, Appl. Surf. Sci. 467—468 (2019) 543—553.

[13] J. Wang, Z. Lu, T. Deng, C. Zhong, Z. Chen, Improved dielectric, nonlinear and magnetic properties of cobalt-doped $CaCu_3Ti_4O_{12}$ ceramics, J. Eur. Ceram. Soc. 38 (2018) 3505—3511.

[14] K. Parida, R.N.P. Choudhary, Structural, electrical, optical and magneto-electric characteristics of chemically synthesized $CaCu_3Ti_4O_{12}$ dielectric ceramics, Mater. Res. Express 4 (2017), 076302.

[15] K. Prompa, E. Swatsitang, T. Putjuso, Very low loss tangent and giant dielectric properties of $CaCu_3Ti_4O_{12}$ ceramics prepared by the sol—gel process, J. Mater. Sci. Mater. Electron. 28 (2017) 15033—15042.

[16] M. Subramanian, D. Li, N. Duan, B.A. Reisner, A.W. Sleight, High dielectric constant in $ACu_3Ti_4O_{12}$ and $ACu_3Ti_3FeO_{12}$ phases, J. Solid State Chem. 151 (2000) 323—325.

[17] X.J. Luo, Y.T. Zhang, D.H. Xu, S.S. Chen, Y. Wang, Y. Chai, Y.S. Liu, S.L. Tang, C.P. Yang, K. Bärner, Origin of the temperature stability of dielectric constant in $CaCu_3Ti_4O_{12}$, Ceram. Int. 45 (2019) 12994—13003.

[18] E. Swatsitang, K. Prompa, T. Putjuso, Ni^{2+}-doped $CaCu_3Ti_4O_{12}/TiO_2$ nano-composite ceramics with high temperature stability dielectric and nonlinear electrical properties for X9R capacitors, Appl. Surf. Sci. 484 (2019) 925—932.

[19] E.C. Grzebielucka, J.F.H. Leandro Monteiro, E.C.F. de Souza, C.P. Ferreira Borges, A.V.C. de Andrade, E. Cordoncillo, H. Beltrán-Mir, S.R.M. Antunes, Improvement in varistor properties of $CaCu_3Ti_4O_{12}$ ceramics by chromium addition, J. Mater. Sci. Technol. 41 (2020) 12—20.

[20] J. Boonlakhorn, P. Kidkhunthod, N. Chanlek, P. Thongbai, (Al^{3+}, Nb^{5+}) co—doped $CaCu_3Ti_4O_{12}$: an extended approach for acceptor—donor hetero-atomic substitutions to achieve high—performance giant—dielectric permittivity, J. Eur. Ceram. Soc. 38 (2018) 137—143.

[21] E. Swatsitang, T. Putjuso, Improved non-ohmic and dielectric properties of Cr^{3+} doped $CaCu_3Ti_4O_{12}$ ceramics prepared by a polymer pyrolysis solution route, J. Eur. Ceram. Soc. 38 (2018) 4994—5001.

[22] X. Yue, W. Long, J. Liu, S. Pandey, S. Zhong, L. Zhang, S. Du, D. Xu, Enhancement of dielectric and non-ohmic properties of graded Co doped $CaCu_3Ti_4O_{12}$ thin films, J. Alloys Compd. 816 (2020) 152582.

[23] P. Cheng, Z. Cao, M. Zhou, Q. Wang, S. Li, J. Liu, Dielectric properties of $CaCu_3Ti_4O_{12}$ ceramics doped by La^{3+}, Ceram. Int. 45 (2019) 15320—15326.

[24] L. Tang, F. Xue, P. Guo, Z. Xin, Z. Luo, W. Li, Significantly enhanced dielectric properties of Y^{3+} donor-doped $CaCu_3Ti_4O_{12}$ ceramics by controlling electrical properties of grains and grain boundaries, Ceram. Int. 44 (2018) 18535—18540.

[25] S. Otatawong, J. Boonlakhorn, S. Danwittayakul, P. Thongbai, $CaCu_3Ti_4O_{12}/In_{0.05}Nb_{0.05}Ti_{0.90}O_{12}$ composite ceramics: an effectively improved method to reduce the dielectric loss tangent and retain high dielectric permittivity, Mater. Res. Bull. 122 (2020) 110700.

[26] S. Kaur, D.P. Singh, On the structural, dielectric and energy storage behaviour of PVDF- $CaCu_3Ti_4O_{12}$ nanocomposite films, Mater. Chem. Phys. 239 (2020) 122301.

[27] A. Haque, D. Ghosh, U. Dutta, A. Shukla, A. Gayen, P. Mahata, A.K. Kundu, M. Motin Seikh, Change in magnetic properties of La_2MnCoO_6 in composite with $CaCu_3Ti_4O_{12}$, J. Magn. Magn Mater. 494 (2020) 165847.

[28] S. Orrego, J.A. Cortés, R.A.C. Amoresi, A.Z. Simões, M.A. Ramírez, Photoluminescence behavior on Sr^{2+} modified $CaCu_3Ti_4O_{12}$ based ceramics, Ceram. Int. 44 (2018) 10781—10789.

[29] R. Parra, E. Longo, M. Cilense, E. Joanni, P.R. Bueno, J.W.M. Espinosa, R. Tararam, J.A. Varela, Photoluminescent $CaCu_3Ti_4O_{12}$-based thin films synthesized by a sol-gel method, J. Am. Ceram. Soc. 91 (2008) 4162—4164.

[30] L.H. Oliveira, A.P. De Moura, F.A. La Porta, I.C. Nogueira, E.C. Aguiar, T. Sequinel, I.L.V. Rosa, E. Longo, J.A. Varela, Influence of Cu-doping on the structural and optical properties of $CaTiO_3$ powders, Mater. Res. Bull. 81 (2016) 1—9.

[31] L.S. Cavalcante, N.C. Batista, T. Badapanda, M.G.S. Costa, M.S. Li, W. Avansi, V.R. Mastelaro, E. Longo, J.W.M. Espinosa, M.F.C. Gurgel, Local electronic structure , optical bandgap and photoluminescence (PL) properties of $Ba(Zr_{0.75}Ti_{0.25})O_3$ powders, Mater. Sci. Semicond. Process. 16 (2013) 1035—1045.

[32] T. Sequinel, I.G. Garcia, S.M. Tebcherani, E.T. Kubaski, L.H. Oliveira, M. Siu Li, E. Longo, J.A. Varela, Red shift and higher photoluminescence emission of CCTO thin films undergoing pressure treatment, J. Alloys Compd. 583 (2014) 488—491.

[33] F. Moura, A.Z. Simões, R.C. Deus, M.R. Silva, J.A. Varela, E. Longo, Intense photoluminescence emission at room temperature in calcium copper titanate powders, Ceram. Int. 39 (2013) 3499—3506.

[34] A.A. Felix, V.D.N. Bezzon, M.O. Orlandi, D. Vengust, M. Spreitzer, E. Longo, D. Suvorov, J.A. Varela, Role of oxygen on the phase stability and micro-structure evolution of $CaCu_3Ti_4O_{12}$ ceramics, J. Eur. Ceram. Soc. 37 (2017) 129—136.

[35] A.A. Felix, M. Spreitzer, D. Vengust, D. Suvorov, M.O. Orlandi, Probing the effects of oxygen-related defects on the optical and luminescence properties in $CaCu_3Ti_4O_{12}$ ceramics, J. Eur. Ceram. Soc. 38 (2018) 5002—5006.

[36] R.J. Holmes, S.R. Forrest, Y.J. Tung, R.C. Kwong, J.J. Brown, S. Garon, M.E. Thompson, Blue organic electrophosphorescence using exothermic host-guest energy transfer, Appl. Phys. Lett. 82 (2003) 2422—2424.

[37] T. Chiba, Y. Hayashi, H. Ebe, K. Hoshi, J. Sato, S. Sato, Y.J. Pu, S. Ohisa, J. Kido, Anion-exchange red perovskite quantum dots with ammonium iodine salts for highly efficient light-emitting devices, Nat. Photon. 12 (2018) 681—687.

[38] P. Vashishtha, M. Ng, S.B. Shivarudraiah, J.E. Halpert, S.B. Shivarudraiah, J.E. Halpert, High efficiency blue and green light-emitting diodes using ruddlesden-popper inorganic mixed halide perovskites with butylammonium interlayers, Chem. Mater. 31 (2019) 83—89.

[39] H.S. Kushwaha, N.A. Madhar, B. Ilahi, P. Thomas, A. Halder, R. Vaish, Efficient solar energy conversion using $CaCu_3Ti_4O_{12}$ photoanode for photocatalysis and photoelectrocatalysis, Sci. Rep. 6 (2016) 1—10.

[40] S. Maity, M. Samanta, A. Sen, K.K. Chattopadhyay, Investigation of

electrochemical performances of ceramic oxide $CaCu_3Ti_4O_{12}$ nanostructures, J. Solid State Chem. 269 (2019) 600−607.

[41] R. Hailili, Z.Q. Wang, Y. Li, Y. Wang, V.K. Sharma, X.Q. Gong, C. Wang, Oxygen vacancies induced visible-light photocatalytic activities of $CaCu_3Ti_4O_{12}$ with controllable morphologies for antibiotic degradation, Appl. Catal. B Environ. 221 (2018) 422−432.

[42] T.A. Otitoju, Y. Li, R. Liu, J. Wang, Y. Ouyang, D. Jiang, S. Li, Polyethersulfone-$CaCu_3Ti_4O_{12}$ hollow fiber membrane with enhanced photocatalytical activity and water permeability, J. Water Process Eng. 33 (2020) 101072.

[43] T.A. Otitoju, D. Jiang, Y. Ouyang, M.A.M. Elamin, S. Li, Photocatalytic degradation of Rhodamine B using $CaCu_3Ti_4O_{12}$ embedded polyethersulfone hollow fiber membrane, J. Ind. Eng. Chem. 83 (2020) 145−152.

[44] Y. Zou, Z. Yuan, S. Bai, F. Gao, B. Sun, Recent progress toward perovskite light-emitting diodes with enhanced spectral and operational stability, Mater. Today Nano. 5 (2019) 100028.

[45] S.D. Stranks, H.J. Snaith, Metal-halide perovskites for photovoltaic and light-emitting devices, Nat. Nanotechnol. 10 (2015) 391−402.

[46] Q. Lin, Z. Wang, H.J. Snaith, M.B. Johnston, L.M. Herz, Hybrid perovskites: prospects for concentrator solar cells, Adv. Sci. 5 (2018) 1−8.

[47] Z.K. Tan, R.S. Moghaddam, M.L. Lai, P. Docampo, R. Higler, F. Deschler, M. Price, A. Sadhanala, L.M. Pazos, D. Credgington, F. Hanusch, T. Bein, H.J. Snaith, R.H. Friend, Bright light-emitting diodes based on organometal halide perovskite, Nat. Nanotechnol. 9 (2014) 687−692.

[48] L. Singh, B.C. Sin, I.W. Kim, K.D. Mandal, H. Chung, Y. Lee, A novel one-step flame synthesis method for tungsten-doped CCTO, J. Am. Ceram. Soc. 99 (2016) 27−34.

[49] P. Thongbai, J. Jumpatam, B. Putasaeng, T. Yamwong, S. Maensiri, The origin of giant dielectric relaxation and electrical responses of grains and grain boundaries of W-doped $CaCu_3Ti_4O_{12}$ ceramics, J. Appl. Phys. 112 (2012).

[50] J.A. Cortés, G. Cotrim, S. Orrego, A.Z. Simões, M.A. Ramírez, Dielectric and non-ohmic properties of $Ca_2Cu_2Ti_{4-x}Sn_xO_{12}$ $(0.0 \leq x \leq 4.0)$ multiphasic ceramic composites, J. Alloys Compd. 735 (2018) 140−149.

[51] H.M. Rietveld, A profile refinement method for nuclear and magnetic structures, J. Appl. Crystallogr. 2 (1969) 65−71.

[52] A.A. Coelho, TOPAS and TOPAS-Academic: an optimization program integrating computer algebra and crystallographic objects written in C++, J. Appl. Crystallogr. 51 (2018) 210−218.

[53] L.B. Mccusker, R.B. Von Dreele, D.E. Cox, D. Louër, P. Scardi, Rietveld refinement guidelines, J. Appl. Crystallogr. 32 (1999) 36−50.

[54] A.M.G. Carvalho, D.H.C. Araújo, H.F. Canova, C.B. Rodella, D.H. Barrett, S.L. Cuffini, R.N. Costa, R.S. Nunes, X-ray powder diffraction at the XRD1 beamline at LNLS, J. Synchrotron Radiat. 23 (2016) 1501−1506.

[55] A.M.G. Carvalho, R.S. Nunes, A.A. Coelho, X-ray powder diffraction of high-Absorption materials at the XRD1 beamline off the best conditions: application to $(Gd, Nd)_5Si_4$ compounds, Powder Diffr. 32 (2017) 10−14.

[56] H.C.N. Tolentino, A.Y. Ramos, M.C.M. Alves, R.A. Barrea, E. Tamura, J.C. Cezar, N. Watanabe, A 2.3 to 25 KeV XAS beamline at LNLS, J. Synchrotron Radiat. 8 (2001) 1040−1046.

[57] B. Ravel, M. Newville, Athena , artemis , HEPHAESTUS : data analysis for X-ray absorption spectroscopy using IFEFFIT, J. Synchrotron Radiat. 12 (2005) 537−541.

[58] A. Bertran, S. Sandoval, J. Oró-Solé, À. Sánchez, G. Tobias, Particle size determination from magnetization curves in reduced graphene oxide decorated with monodispersed superparamagnetic iron oxide nanoparticles, J. Colloid Interface Sci. 566 (2020) 107−119.

[59] A.C. Sparavigna, On the use of ImageJ segmentation, Zenodo Repos (2020) 1−11.

[60] B.G. Dick, A.W. Overhauser, Theory of the dielectric constants of alkali halide crystals, Phys. Rev. 112 (1958) 90−103.

[61] B. Hadjarab, A. Bouguelia, M. Trari, Synthesis , physical and photo electrochemical characterization of La-doped $SrSnO_3$, J. Phys. Chem. Solid. 68 (2007) 1491−1499.

[62] J.D. Gale, GULP: a computer program for the symmetry-adapted simulation of solids, Faraday 93 (1997) 629−637.

[63] P. Dorenbos, A review on how lanthanide impurity levels change with chemistry and structure of inorganic compounds, ECS J. Solid State Sci. Technol. 2 (2013) R3001−R3011.

[64] S. Zhang, Z. Song, S. Wang, Z. Wang, F. Wang, Q. Liu, Red persistent and photostimulable phosphor $SrLiAl_3N_4:Eu^{2+}$, J. Mater. Chem. C. 8 (2020) 4956−4964.

[65] A. Bril, A.W. de Jager-Veenis, Some methods of luminescence efficiency measurements, J Res Natl Bur Stand Sect A Phys Chem 80 (1976) 401−407.

[66] J. Thomas, GoCIE V2., 2009.

[67] C.S. McCamy, Correlated color temperature as an explicit function of chromaticity coordinates, Color Res. Appl. 17 (1992) 142−144.

[68] R.D. Shannon, Revised effective ionic radii and systematic studies of interatomic distances in halides and chalcogenides, Acta Crystallogr. A32 (1976) 751−767.

[69] Z. Song, J. Zhao, Q. Liu, Luminescent perovskites: recent advances in theory and experiments, Inorg. Chem. Front. 6 (2019) 2969−3011.

[70] P.Y. Raval, N.P. Joshi, P.R. Pansara, N.H. Vasoya, S. Kumar, S.N. Dolia, K.B. Modi, R.K. Singhal, A Ti L3,2 - and K- edge XANES and EXAFS study on $Fe3+$ - substituted $CaCu_3Ti_4O_{12}$, Ceram. Int. 44 (2018) 20716−20722.

[71] X. Liu, Z. Song, Y. Kong, S. Wang, S. Zhang, Z. Xia, Q. Liu, Effects of full-range Eu concentration on $Sr_{2-2x}Eu_{2x}Si_5N_8$ phosphors: a deep-red emission and luminescent thermal quenching, J. Alloys Compd. 770 (2019) 1069−1077.

[72] U.M. Meshiya, P.Y. Raval, P.R. Pansara, M. Nehra, N. Jakhar, S. Kumar, K.B. Modi, D.-K. Lim, R.K. Singhal, Electronic structure, orbital symmetry transformation, charge transfer, and valence state studies on Fe^{3+}-substituted $CaCu_3Ti_4O_{12}$ quadruple perovskites using X-ray photoelectron spectroscopy, Ceram. Int. 46 (2020) 2147−2154.

[73] J. Jumpatam, Giant dielectric behavior of monovalent cation/anion (Li^+, F^-) co-doped $CaCu_3Ti_4O_{12}$ ceramics, J. Am. Ceram. Soc. 103 (2020) 1871−1880.

[74] J. Jumpatam, N. Chanlek, P. Thongbai, Giant dielectric response, electrical properties and nonlinear current-voltage characteristic of Al_2O_3-$CaCu_3Ti_4O_{12}$ nanocomposites, Appl. Surf. Sci. 476 (2019) 623−631.

[75] C.R. Foschini, B. Hangai, P.P. Ortega, E. Longo, M. Cilense, A.Z. Simões, Evidence of ferroelectric behaviour in $CaCu_3Ti_4O_{12}$ thin films deposited by RF-sputtering, Process, Appl. Ceram. 13 (2019) 219−228.

[76] N. Kolev, R.P. Bontchev, A.J. Jacobson, V.N. Popov, V.G. Hadjiev, A.P. Litvinchuk, M.N. Iliev, Raman spectroscopy of $CaCu_3Ti_4O_{12}$, Phys. Rev. B Condens. Matter 66 (2002) 1−4.

[77] D. Valim, A.G. Souza Filho, P.T.C. Freire, S.B. Fagan, A.P. Ayala, J. Mendes Filho, A.F.L. Almeida, P.B.A. Fechine, A.S.B. Sombra, J. Staun Olsen, L. Gerward, Raman scattering and x-ray diffraction studies of polycrystalline $CaCu_3Ti_4O_{12}$ under high-pressure, Phys. Rev. B Condens. Matter 70 (2004) 2−5.

[78] Y. Tezuka, Y. Yokouchi, S. Sasaki, S. Nakamoto, K. Nishiyama, M. Mikami, H.J. Im, T. Watanabe, S. Nozawa, N. Nakajima, T. Iwazumi, Electronic structure study of $CaCu_3Ti_4O_{12}$ by means of X-ray Raman scattering, J. Electron. Spectrosc. Relat. Phenom. 220 (2017) 114−117.

[79] S.P.S. Porto, J.F. Scott, Raman spectra of $CaWO_4$, $SrWO_4$, $CaMoO_4$, and $SrMoO_4$, Phys. Rev. 157 (1967) 716−719.

[80] J. Suda, T. Sato, Temperature depedence of the linewidth of the first-order Raman spectra for $CaWO_4$ crystal, J. Phys. Soc. Japan. 66 (1997) 1707−1713.

[81] L. Gracia, V.M. Longo, L.S. Cavalcante, A. Beltrn, W. Avansi, M.S. Li, V.R. Mastelaro, J.A. Varela, E. Longo, J. Andrés, Presence of excited electronic state in $CaWO_4$ crystals provoked by a tetrahedral distortion: an experimental and theoretical investigation, J. Appl. Phys. 110 (2011), 043501.

[82] J. Lv, E. Xiao, X. Li, X. Dong, Y. Chen, Z. Yue, F. Shi, Crystal structures, dielectric properties, and lattice vibrational characteristics of $(1-x)CaWO_4$- $xTiO_2$ composite ceramics, Ceram. Int. 46 (2020) 3715−3724.

[83] S.A. Abdullah, M.Z. Sahdan, N. Nayan, Z. Embong, C.R.C. Hak, F. Adriyanto, Neutron beam interaction with rutile TiO_2 single crystal (111): Raman and XPS study on Ti^{3+}-oxygen vacancy formation, Mater. Lett. 263 (2020) 127143.

[84] X. Li, C. Chen, F. Zhang, X. Huang, Z. Yi, Giant photostriction of $CaCu_3Ti_4O_{12}$ ceramics under visible light illumination, Appl. Phys. Lett. 116 (2020) 4−9.

[85] R.V. Vendrinsckii, V.L. Kraizman, A.A. Novakovich, P.V. Demekhin, S.V. Urazhdin, Pre-edge fine structure of the 3d atom K X-ray absorption spectra and quantitative atomic structure determinations for ferroelectric perovskite structure crystals, J. Phys. Condens. Matter 10 (1998) 9561.

[86] F. Farges, G.E. Brown, J.J. Rehr, Ti K -edge XANES studies of Ti coordination and disorder in oxide compounds : comparison between theory and experiment, Phys. Rev. B 56 (1997) 1809−1819.

[87] V. Krayzman, I. Levin, J.C. Woicik, D. Yoder, D.A. Fischer, Effects of local atomic order on the pre-edge structure in the Ti K x-ray absorption spectra of perovskite $CaTi_{1-x}Zr_xO_3$, Phys. Rev. B 74 (2006) 224104.

[88] S. De Lazaro, J. Milanez, A.T. de Figueiredo, V.M.V.M. Longo, V.R. Mastelaro, F.S. De Vicente, A.C. Hernandes, J.A.J.A. Varela, E. Longo, Relation between photoluminescence emission and local order-disorder in the $CaTiO_3$ lattice modifier, Appl. Phys. Lett. 90 (2007) 9−12.

[89] C. Ribeiro, C. Vila, D.B. Stroppa, V.R. Mastelaro, J. Bettini, E. Longo, E.R. Leite, Anisotropic growth of oxide nanocrystals: insights into the rutile TiO_2 phase, J. Phys. Chem. C 111 (2007) 5871−5875.

[90] K. Li, D. Xue, Estimation of electronegativity values of elements in different valence states, J. Phys. Chem. 110 (2006) 11332−11337.

[91] Y. Zhu, T. Wang, W. Wang, S. Chen, E. Lichtfouse, C. Cheng, J. Zhao, Y. Li, C. Wang, $CaCu_3Ti_4O_{12}$, an efficient catalyst for ibuprofen removal by activation of peroxymonosulfate under visible-light irradiation, Environ. Chem. Lett. 17 (2019) 481−486.

[92] L.F. Da Silva, W. Avansi, M.L. Moreira, A. Mesquita, L.J.Q. Maia, J. Andrés, E. Longo, V.R. Mastelaro, Relationship between crystal shape, photoluminescence, and local structure in $SrTiO_3$ synthesized by microwave-assisted hydrothermal method, J. Nanomater. 2012 (2012) 25−28.

[93] G.J. Barbosa Junior, A.M. Sousa, S.M. de Freitas, R.D.S. Santos, M.V. do, S. Rezende, Investigation of Europium dopant in the orthophosphate $KMPO_4$ (M = Ba and Sr) compounds, J. Phys. Chem. Solid. 130 (2019) 282−289.

[94] S.M. de Freitas, G.J.B. Júnior, R.D.S. Santos, M.V.S. Rezende, Defects and dopant properties of $SrSnO_3$ compound: a computational study, Comput. Condens. Matter. 21 (2019), e00411.

[95] S.M. de Freitas, M.V.S. Rezende, Effect of europium concentration on its distribution in the host sites of lithium tantalate, J. Phys. Chem. Solid. 112 (2018) 158−162.

[96] M.A. Ramirez, P.R. Bueno, J.A. Varela, E. Longo, Non-Ohmic and dielectric properties of a $Ca_2Cu_2Ti_4O_{12}$ polycrystalline system, Appl. Phys. Lett. 89 (2006) 87−90.

[97] L.H. Oliveira, M.A. Ramírez, M.A. Ponce, L.A. Ramajo, A.R. Albuquerque, J.R. Sambrano, E. Longo, M.S. Castro, F.A. La Porta, Optical and gas-sensing properties, and electronic structure of the mixed-phase $CaCu_3Ti_4O_{12}$/$CaTiO_3$ composites, Mater. Res. Bull. 93 (2017) 47−55.

[98] T. Badapanda, S.K. Rout, L.S. Cavalcante, J.C. Sczancoski, S. Panigrahi, E. Longo, M.S. Li, Optical and dielectric relaxor behaviour of Ba(Zr$_{0.25}$Ti$_{0.75}$)O$_3$ ceramic explained by means of distorted clusters, J. Phys. D Appl. Phys. 42 (2009) 175414.

[99] L.S. Cavalcante, J.C. Sczancoski, J.W.M. Espinosa, V.R. Mastelaro, A. Michalowicz, P.S. Pizani, F.S. De Vicente, M.S. Li, J.A. Varela, E. Longo, Intense blue and green photoluminescence emissions at room temperature in barium zirconate powders, J. Alloys Compd. 471 (2009) 253−258.

[100] H.W. Eng, P.W. Barnes, B.M. Auer, P.M. Woodward, Investigations of the electronic structure of d0 transition metal oxides belonging to the perovskite family, J. Solid State Chem. 175 (2003) 94−109.

[101] L.H. Oliveira, E.C. Paris, W. Avansi, M.A. Ramirez, V.R. Mastelaro, E. Longo, J.A. Varela, Correlation between photoluminescence and structural defects in Ca$_{1+x}$Cu$_{3-x}$Ti$_4$O$_{12}$ systems, J. Am. Ceram. Soc. 96 (2013) 209−217.

[102] A. Noori, P. Mahbub, M. Dvořák, A. Lucieer, M. Macka, Radiometric analysis of UV to near infrared LEDs for optical sensing and radiometric measurements in photochemical systems, Sensor. Actuator. B Chem. 262 (2018) 171−179.

[103] Z. Wang, Z. Jia, Q. Li, X. Zhang, W. Sun, J. Sun, B. Liu, B. Ha, The enhanced NO$_2$ sensing properties of SnO$_2$ nanoparticles/reduced graphene oxide composite, J. Colloid Interface Sci. 537 (2019) 228−237.

[104] L. Dong, E. Zhao, Y. Chen, G. Qin, W. Xu, Impact of LED color temperatures on perception luminance in the interior zone of a tunnel considering fog transmittance, Adv. Civ. Eng. 2020 (2020).

[105] G.L. Miller, D.V. Lang, L.C. Kimerling, Capacitance transient spectroscopy, Mater. Sci. 7 (1977) 377−448.

[106] F.D. Auret, P.N.K. Deenapanray, Deep level transient spectroscopy of defects in high-energy light-particle irradiated Si, Crit. Rev. Solid State Mater. Sci. 29 (2004) 1−44.

[107] A. Hallén, M. Bakowski, Combined proton and electron irradiation for improved GTO thyristors, Solid State Electron. 32 (1989) 1033−1037.

[108] M.L. Moreira, E.C. Paris, G.S. do Nascimento, V.M. Longo, J.R. Sambrano, V.R. Mastelaro, M.I.B. Bernardi, J. Andrés, J.A. Varela, E. Longo, Structural and optical properties of CaTiO$_3$ perovskite-based materials obtained by microwave-assisted hydrothermal synthesis: an experimental and theoretical insight, Acta Mater. 57 (2009) 5174−5185.

[109] S. Wang, H. Gao, G. Sun, Y. Li, Y. Wang, H. Liu, C. Chen, Liang Yang, Structure characterization, optical and photoluminescence properties of scheelite-type CaWO$_4$ nanophosphors: effects of calcination temperature and carbon skeleton, Opt. Mater. 99 (2020) 109562.